

**©Copyright**

**by**

**Adrian Ioan Ciucivara**

**2007**

**The Dissertation Committee for Adrian Ioan Ciucivara**

**certifies that this is the approved version of the following dissertation:**

**DENSITY FUNCTIONAL STUDIES OF MAGNETIC  
SEMICONDUCTORS AND MULTIFERROICS**

**Committee:**

---

**Leonard Kleinman, Supervisor**

---

**Alexander A. Demkov**

---

**Zhen Yao**

---

**James L. Erskine**

---

**Allan H. MacDonald**

---

**Sanjay K. Banerjee**

**DENSITY FUNCTIONAL STUDIES OF MAGNETIC  
SEMICONDUCTORS AND MULTIFERROICS**

by

**Adrian Ioan Ciucivara, B.S.; M.S.**

**Dissertation**

Presented to the Faculty of the Graduate School of

The University of Texas at Austin

In Partial Fulfillment

of the Requirements

for the Degree of

**Doctor of Philosophy**

The University of Texas at Austin

December 2007

*to my father*

IANIK

# Acknowledgement

I would like to express my deep and sincere gratitude to my supervisor, Professor Leonard Kleinman for his guidance, and support during the entire period of my PhD work.

I thank Professor Alexander A. Demkov, for many helpful discussions and suggestions and his positive attitude and optimism.

I thank Dr. B. R. Sahu for his personal guidance and suggestions on many topics.

I warmly thank Professor Mrinal Sen for introducing and encouraging me to work on inverse theory problems in geophysics over my summer internships.

My sincere thanks are due to all committee members: Prof. Allan. H. MacDonald, Prof. Sanjay Banerjee, Prof. Zhen Yao and Prof. James Erskine.

Finally, I would like to thank my friends Manish Niranjana, Muhammad N. Huda and Priya Gopal who always kept the atmosphere cheerful with their warm presence.

Adrian Ioan Ciucivara

*The University of Texas at Austin*

*December 2007*

# DENSITY FUNCTIONAL STUDIES OF MAGNETIC SEMICONDUCTORS AND MULTIFERROICS

Publication No. \_\_\_\_\_

Adrian Ioan Ciucivara, Ph.D.

The University of Texas at Austin, 2007

Supervisor: Leonard Kleinman

The present work is mostly focused on theoretical study of multiferroics and magnetic semiconductors within the framework of density functional theory (DFT). We studied  $\text{Bi}_2\text{NiMnO}_6$  which was recently synthesized as a heavily distorted double perovskite with four formula units in a monoclinic unit cell. The calculated GGA and GGA+U magnetizations per formula unit were 4.92 and 4.99  $\mu_B$  and the calculated ferroelectric polarizations were 16.83 and 16.63  $\mu\text{C cm}^{-2}$ . We also present the results of completely relaxed electronic structure calculations for multiferroic  $\text{LaMnO}_3/\text{BaTiO}_3$  structure which was built by joining a slab of magnetic  $\text{LaMnO}_3$  with a slab of ferroelectric  $\text{BaTiO}_3$ . The study of Mn doped GeTe, which is a diluted magnetic semiconductor (DMS), shows the net magnetization as a function of doping and holes concentration. In addition, we present a study of ferroelectric GeTe as a function of applied pressure and the interesting properties exhibited by Si(001)/Si(110) junction which was experimentally built using hybrid orientation technology (HOT).

# TABLE OF CONTENTS

Acknowledgement	iv
Abstract	v
List of Tables	vii
List of Figures	viii
<b>CHAPTER 1 INTRODUCTION</b>	<b>1</b>
<b>1.1 Ferroelectricity</b>	<b>3</b>
1.1.1 Polarization Catastrophe.	4
1.1.2 Landau theory of phase transition.	7
1.1.3 Berry phase and modern theory of polarization	9
<b>1.2 Magnetism</b>	<b>13</b>
<b>1.3 Methodology and framework</b>	<b>15</b>
1.3.1 Basic equations for interacting electrons and nuclei	15
1.3.2 Density Functional Theory (DFT)	18
<b>CHAPTER 2 THE EFFECT OF PRESSURE ON GETE</b>	<b>24</b>
<b>2.1 Computational details</b>	<b>25</b>
<b>2.2 Discussion of the results</b>	<b>27</b>
<b>2.3 Conclusion</b>	<b>36</b>
<b>CHAPTER 3 DFT STUDY OF MULTIFERROIC BI<sub>2</sub>NIMNO<sub>6</sub></b>	<b>38</b>
<b>3.1 Computational Method and Crystal Symmetry.</b>	<b>41</b>
<b>3.2 Results and Discussions.</b>	<b>44</b>

<b>CHAPTER 4</b>	<b>DFT STUDY OF BATIO<sub>3</sub>-LAMNO<sub>3</sub> HETEROSTRUCTURE</b>	<b>51</b>
4.1	Computational Details	54
4.2	Results and Discussion	55
<b>CHAPTER 5</b>	<b>DFT STUDY OF GE<sub>1-x</sub>MN<sub>x</sub>TE</b>	<b>60</b>
5.1	Computational Details	61
5.2	Results and Comparison with Experiment	62
<b>CHAPTER 6</b>	<b>DFT STUDY OF SI-SI INTERFACES</b>	<b>72</b>
6.1	Calculations and results	73
<b>REFERENCES</b>		<b>82</b>
<b>VITA</b>		<b>93</b>



## List of Tables

<i>Table 1.1: Compilation of data on ferroelectric materials.....</i>	<i>4</i>
<i>Table 2.1.1: Convergence parameters and the effect on the energy.....</i>	<i>26</i>
<i>Table 2.2.1: Comparison of LDA and GGA trigonal GeTe results with experiment.....</i>	<i>27</i>
<i>Table 2.2.3: Polarization effective charge <math>Z^*</math>.....</i>	<i>30</i>
<i>Table 2.2.2: Trigonal and cubic GeTe quantities as a function of applied pressure.....</i>	<i>33</i>
<i>Table 2.2.4: Comparison of enthalpy vs. energy based critical parameters.....</i>	<i>35</i>
<i>Table 3.1.1: Space group symmetry of the crystal.....</i>	<i>44</i>
<i>Table 3.2.1: Lattice constants, angles and cohesive energies.....</i>	<i>45</i>
<i>Table 3.2.2: Calculated atomic positions.....</i>	<i>45</i>
<i>Table 3.2.3: Magnetic moments in <math>\mu_B</math> per formula unit.....</i>	<i>47</i>
<i>Table 3.2.4: The GGA and GGA+U electric polarizations.....</i>	<i>49</i>
<i>Table 4.2.1: Lattice constants.....</i>	<i>55</i>
<i>Table 4.2.2: Magnetization per manganese.....</i>	<i>56</i>
<i>Table 4.2.3: Mn-O bond lengths.....</i>	<i>57</i>
<i>Table 4.2.4: Polarization results.....</i>	<i>59</i>
<i>Table 5.2.1: Compilation of the experimental magnetization in <math>\mu_B</math> per Mn for various compositions and number of carriers per <math>cm^3</math>.....</i>	<i>63</i>
<i>Table 5.2.2: Average lattice angles and lattice constants.....</i>	<i>64</i>
<i>Table 5.2.3: Total and projected magnetizations in <math>\mu_B</math> per Mn.....</i>	<i>65</i>
<i>Table 6.1.1: Important quantities which describe the interface.....</i>	<i>77</i>

## LIST OF FIGURES

<i>Fig. 1.1.3: Different choices for a unit cell give rise to different dipole moments.</i> .....	10
<i>Fig. 1.3.2a: Schematic representation of Hohenberg-Khan theorem.</i> .....	18
<i>Fig. 1.3.2b: Flowchart of self-consistent Kohn-Sham calculation.</i> .....	22
<i>Fig. 2.2.1: Energy bands of rhombohedral GeTe.</i> .....	29
<i>Fig. 2.2.2: Plot of the pseudocharge density along the nearest neighbor direction in trigonal GeTe.</i> .....	31
<i>Fig. 2.2.3: Identical to Fig. 2.2.2 except that the plot is along the 3-fold axis.</i> .....	32
<i>Fig. 2.2.4: Cohesive energy vs. volume plots for rock salt and rhombohedral GeTe.</i> ...	34
<i>Fig. 3.1.1: Unit cell of <math>\text{Bi}_2\text{NiMnO}_6</math> containing four formula units.</i> .....	43
<i>Fig. 3.2.1: Density of states.</i> .....	46
<i>Fig. 4.2.1: Polarization as a function of displacement.</i> .....	58
<i>Fig. 5.2.1: Total and projected Mn d densities of states.</i> .....	67
<i>Fig. 5.2.2 Energy bands around the energy gap for the values of x and v shown.</i> .....	69
<i>Fig. 5.2.3: Hole Fermi energies vs. hole density per <math>\text{cm}^3</math>.</i> .....	70
<i>Fig. 6.1: Current vs. voltage curve for a Si(110)/Si(001) junction.</i> .....	72
<i>Fig. 6.1.1: The Si(110)/Si(001) unrelaxed interfaces for 2 different orientations.</i> .....	73
<i>Fig. 6.1.2: (a) Unrelaxed and (b) relaxed Si(110)/Si(001) interface planes and (c) a side view of the relaxed interface.</i> .....	75
<i>Fig. 6.1.3: Same as Fig. 3 except for Si(110)/Si(100).</i> .....	76
<i>Fig. 6.1.4: Planar average of the coulomb plus exchange-correlation potential for (a) Si(110)/Si(001) and (b) Si(110)/Si(100) supercells.</i> .....	78
<i>Fig. 6.1.5: Energy bands around the Fermi energy of Si(110)/Si(001).</i> .....	79
<i>Fig. 6.1.6: Interface states at <math>k = \pi/2a</math> for the (a) 268th band, (b) 258<sup>th</sup> band, and (c) 259<sup>th</sup> bands of Si(110)/Si(001).</i> .....	80
<i>Fig. 6.1.7: Si(001)/Si(100) energy bands in eV away from the top of the valence bands.</i> .....	81

# Chapter 1 Introduction

Multiferroic materials form a class of compounds which have recently gained a lot of attention from the material physics community. In order for a compound to belong to this group, it requires at least two order parameters to coexist in the same phase. Considering properties like elasticity, ferroelectricity and ferromagnetism, there are three distinct groups of multiferroics: piezoelectrics, which have elastic and electric properties, piezomagnets, which have elastic and magnetic properties and magnetoelectrics, where the ferroelectric and ferromagnetic properties coexist. If the first two groups of multiferroics are relatively common, the magnetoelectric materials are much more elusive. There exist relatively few magnetoelectric multiferroics, and most of those are antiferromagnetic. They form a fascinating field of study which can be framed by two questions asked by Nicola Spaldin (nee Hill) <sup>1-4</sup>, “Why are there so few magnetic ferroelectrics?” and “Why are there any magnetic ferroelectrics?”

Ferromagnetic ferroelectric multiferroic materials appear to have great potential for device applications. If the magnetization  $M$  and the electric polarization  $P$  are uncoupled, they can be used to encode four different logic states. For example, Gajek *et al.*<sup>5</sup> have reported using 2 nm thick films of  $\text{La}_{0.1}\text{Bi}_{0.9}\text{MnO}_3$  as spin filtering tunnel barriers, the magnetization and electric polarization of which can be switched independently, giving rise to four different resistance states.

Another class of materials that is receiving a lot of attention from condensed matter physicists is the one formed by diluted magnetic semiconductors simply known as DMS.

Diluted magnetic semiconductors (DMS) have been intensely studied because of their potential technological applications. The two important properties, that make DMS's so interesting, are their ferromagnetism and their semiconductor nature. A microdevice realized from a DMS, would have the tunability of a semiconductor (controlled by a gate voltage) and also memory storage capabilities due to its ferromagnetic nature. Even though this is a technological direction of great importance there remain obstacles such as weak ferromagnetic ordering and Curie temperatures, which are, in most of the cases, far below room temperature.

The present work is organized as follows:

- The subsections in the introduction briefly discuss ferroelectricity and magnetism and also present the main equations and the framework used for the calculations related to current work.
- Chapter 2 is a thorough discussion on the ferroelectric GeTe.
- Chapter 3 presents the results of our DFT calculations on multiferroic  $\text{Bi}_2\text{NiMnO}_6$ .
- Chapter 4 presents the results of our DFT calculations on multiferroic superlattice structure built by joining a slab of magnetic  $\text{LaMnO}_3$  with a slab of ferroelectric  $\text{BaTiO}_3$ .
- Chapter 5 is a discussion on the Mn doped GeTe which is a diluted magnetic semiconductor (DMS).
- Chapter 6 presents our DFT calculation results on Si(001)/Si(110) junction which was experimentally built using hybrid orientation technology (HOT) and exhibits very interesting properties.

## 1.1 Ferroelectricity

Ferroelectric materials can be characterized from the viewpoint of a special structural phase transition, called ferroelectric transition. This is associated with the appearance of a spontaneous dielectric polarization in the crystal even in the absence of an external electric field. This polarization is due to the fact that the center of the positive charges does not coincide with the center of the negative ones. Similar to the magnetic polarization, the electric one is associated with a hysteresis loop. Also, the materials that belong to this group usually have a Curie temperature  $T_c$ , above which the electric order is destroyed due to a high thermal energy of the crystal lattice. There are cases where  $T_c$  is not defined only because it is higher than the melting temperature of the compound.

In the table below the commonly considered ferroelectrics are listed along with their  $T_c$  and the spontaneous polarization,  $P_s$ , as they were compiled by Subbarao<sup>1</sup>. The last column represents the temperature at which the polarization was measured.

Type	Formula	$T_c$ (K)	$P_s$ ( $\mu\text{C cm}^{-2}$ )	T (K)
	GeTe	670	-	-
<b>KDP</b>	$\text{KH}_2\text{PO}_4$	123	4.75	96
	$\text{KD}_2\text{PO}_4$	213	4.83	180
	$\text{KH}_2\text{AsO}_4$	97	5.00	78
<b>TGS</b>	Tri-glycine sulfate	322	2.8	29
	Tri-glycine selenate	295	3.2	283
<b>Perovskites</b>	$\text{BaTiO}_3$	408	26.0	296
	$\text{KNbO}_3$	708	30.0	523

	PbTiO <sub>3</sub>	765	>50	296
	LiTaO <sub>3</sub>	938	50	-
	LiNbO <sub>3</sub>	1480	71	296

*Table 1.1: Compilation of data on ferroelectric materials.*

In the table above, the ferroelectrics were classified by their chemical formula. A more important classification is based on the mechanism that is responsible for the transition. Based on this criterion, there are two main classes of ferroelectrics:

- displacive type, if in paraelectric phase, the atoms oscillate about a nonpolar site while in the ferroelectric phase they oscillate about a polar site.
- order-disorder type, if in paraelectric phase, the atoms oscillate about a double-well or multi-well configuration of sites while in the ferroelectric phase they oscillate about an ordered subset of these wells.

In the next subsections I will briefly present three of the theories that will explain ferroelectricity from different viewpoints.

### **1.1.1 Polarization Catastrophe.**

A viewpoint that contributes to the understanding of the ferroelectric displacive transition is the polarization catastrophe in which under some critical condition, the polarization or some fourier components of the polarization become very large. This is due to the fact that the electric field created by the ionic displacement is larger than the

elastic restoring forces. The displacements will converge to some finite values due to the higher order approximations in the elastic forces.

The simple form of polarization catastrophe theory is achieved by considering that the local field of all atoms has the form:

$$E_{local} = E + \frac{4\pi}{3}P \quad (1.1.1.1)$$

where  $E$  is the macroscopic field and  $P$  is the polarization of the crystal which, can be written as a function of the polarizabilities of the atoms times the local electric field:

$$P = \sum_j N_j p_j = \sum_j N_j \alpha_j E_{local}(j) \quad (1.1.1.2)$$

Here  $N_j$  represents the concentration,  $\alpha_j$  is the polarizability of atom  $j$ , and  $E_{local}(j)$  is the local field at atom site  $j$ . Our goal is to relate the dielectric constant  $\epsilon$ , to the polarizabilities. The dielectric constant  $\epsilon$  for an isotropic medium is defined in terms of the macroscopic field  $E$  by the following expression:

$$\epsilon = \frac{E + 4\pi P}{E} \quad (1.1.1.3)$$

Combining equation (1.1.1.1) and (1.1.1.2) the expression for  $P$  becomes:

$$P = \left( \sum_j N_j \alpha_j \right) \left( E + \frac{4\pi}{3} P \right) \quad (1.1.1.4)$$

Inverting this equation for  $E$  and replacing the expression in (1.1.1.3) we get an expression for  $\epsilon$  as a function only of polarizability and concentration:

$$\varepsilon = \frac{1 + \frac{8\pi}{3} \sum_j N_j \alpha_j}{1 - \frac{4\pi}{3} \sum_j N_j \alpha_j} \quad (1.1.1.5)$$

Analyzing this expression, it is obvious that the dielectric constant has a singularity and becomes infinite for  $\sum_j N_j \alpha_j = 3/4\pi$ . This is precisely the condition for a polarization catastrophe. The physical interpretation of the fact that the dielectric constant becomes infinite if the above equality was fulfilled is the nonferroelectric-ferroelectric phase transition. It is easy to see that  $\varepsilon$  is very sensitive to small displacements of  $\sum_j N_j \alpha_j$  from the critical value  $3/4\pi$ . If  $s$  is a measure of the displacement with  $s \ll 1$ , then we can write:

$$(4\pi/3) \sum_j N_j \alpha_j = 1 - 3s \quad (1.1.1.6)$$

Replacing this expression in (1.1.1.5), we find for the dielectric:

$$\varepsilon = \frac{1-s}{s} \approx \frac{1}{s} \quad (1.1.1.7)$$

If we define  $s$  as a linear function of the temperature around the critical temperature point  $T_c$ , we can write:

$$s = \frac{(T - T_c)}{\xi} \quad (1.1.1.8)$$

where  $\xi$  is a constant. From(1.1.1.8), the expression for the dielectric constant becomes:

$$\varepsilon = \frac{\xi}{(T - T_c)} \quad (1.1.1.9)$$



This expression is in a fairly good agreement with the observed temperature variation in paraelectric state.

### 1.1.2 Landau theory of phase transition.

The ferroelectric-paraelectric phase transition can be either a second order transition, where the order parameter goes to zero without a discontinuity when the temperature raises above the critical temperature, like the ferromagnetic-paramagnetic or normal-superconducting transition, or a first order transition, which presents a discontinuous change in the order parameter. A consistent formal theory of the behavior of a ferroelectric can be accomplished by expanding the free energy of the crystal in powers of the polarization, expansion first proposed by Landau:

$$F(P, T, E) = -EP + g_0 + \frac{1}{2}g_2P^2 + \frac{1}{4}g_4P^4 + \frac{1}{6}g_6P^6 + \dots \quad (1.1.2.1)$$

where the coefficients  $g$  are temperature dependent and the odd powers of the polarization in the Taylor expansion are zero if the crystal has a center of inversion symmetry. In thermal equilibrium the value of  $P$  is determined by the solution that minimizes the free energy. This means that the derivative of the free energy function with respect to the polarization has to be zero:

$$\frac{\partial F(P, T, E)}{\partial P} = 0 = -E + g_2P + g_4P^3 + g_6P^5 + \dots \quad (1.1.2.2)$$

In order to get a ferroelectric specimen, the coefficient of  $P$ ,  $g_2$ , from (1.1.2.2) has to go through zero at some critical temperature. A suitable form for  $g_2$  would be:

$$g_2 = \gamma(T - T_c) \quad (1.1.2.3)$$

where  $\gamma$  is a positive constant. We can see that for a small positive value of  $\gamma$  the crystal is close to instability while for a negative value the unpolarized lattice is unstable.

Analyzing the solution for equation (1.1.2.2), there are two different cases depending on the sign of  $g_4$ . If  $g_4$  is a positive value then we can ignore  $g_6$  which doesn't bring any new addition to the solution and the equation that remains to be solved for zero external electric field is:

$$\gamma(T - T_c)P + g_4P^3 = 0 \quad (1.1.2.4)$$

This equation has two different solutions depending on the temperature domain. For temperatures larger than  $T_c$  the solution is  $P = 0$  while for the lower temperature domain  $P = (\gamma / g_4)^{1/2} (T - T_c)^{1/2}$ . Analyzing the expression of the polarization for the ferroelectric phase, we can see that the ferroelectric-paraelectric transition is a second order transition because the polarization approaches zero smoothly (square root dependence) when the temperature approaches the Curie temperature  $T_c$ .  $\text{LiTaO}_3$  is an example of a ferroelectric with a second order phase transition.

Now, if we consider the case where  $g_4$  has a negative value then we have to retain  $g_6$ . The new equation to solve becomes:

$$\gamma(T - T_c)P - |g_4|P^3 + g_6P^5 = 0 \quad (1.1.2.5)$$

This has the obvious solution  $P = 0$  for paraelectric regime, and for the ferroelectric regime the polarization has to obey the following equation for  $P$ :

$$\gamma(T - T_c) - |g_4|P^2 + g_6P^4 = 0 \quad (1.1.2.6)$$

Depending on the  $g$  coefficients, the value of the solution of (1.1.2.6) which minimizes (1.1.2.5), can be a nonzero positive value of the polarization even in the vicinity of the critical temperature approaching from below. At the same time, approaching from above,

$T_c$  the polarization is zero as shown. That means there is a gap in the polarization at the Curie temperature that makes this type of transition a first order phase transition. An example of a ferromagnet that belongs to this group is  $\text{BaTiO}_3$ .

### 1.1.3 Berry phase and modern theory of polarization

So far, the two theories discussed in the previous subsections, Polarization catastrophe and Landau theory of phase transition, explained qualitatively why, for some special conditions, some materials may exhibit a net polarization in a zero electric field. A quantitative discussion though, may turn out being quite challenging in the case of infinite or extended systems. If the system is finite, there is no problem for defining the average value of the polarization as follow in term of the total dipole moment  $d$ :

$$P \equiv \frac{d}{\Omega} = \frac{1}{\Omega} \int_{\Omega} dr n(r)r \quad (1.1.3.1)$$

The integral in (1.1.3.1) is a well defined integral since the density vanishes outside the system and there is no problem with the integrand  $n(r)r$ . The problem is subtler for an extended system. In this situation we try to identify the bulk intrinsic polarization and the best choice to specify the bulk polarization is to require the external macroscopic field to vanish. This is the only well defined reference<sup>2,3</sup> as long as the bulk is not interacting with external charges at long distances. The fact that the electrons in a crystal move in a periodic potential simplifies the problem to some extent but there are still further complications which arise from the fact that there is not a unique way to choose the unit cell. This issue is emphasized in Fig. 1.1.3.1 where it is clear that even for a simple 2-

dimensional array of alternating charges the choice for choosing a unit cell is not unique, which gives completely different polarizations for different choices.

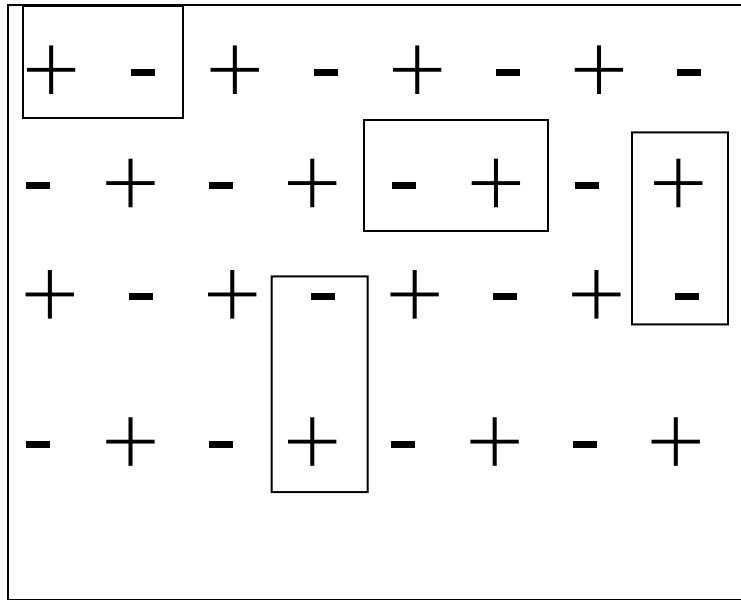


*Fig. 1.1.3: Different choices for a unit cell give rise to different dipole moments.*

Another issue is related to the quantum nature of the electronic charges that form a continuous distribution. This continuous distribution will make any attempt to divide the 3- dimensional charge distribution in a unique periodic array<sup>4</sup> impossible. The answer to this fairly complicated problem comes from a fully quantum mechanical treatment. A recent breakthrough was made when people realized that the geometrical berry phase<sup>5</sup> can be intimately related with the intrinsic polarization of the bulk<sup>6,7</sup>. To show this we can write the change in the polarization as follows:

$$\Delta P = \int_0^1 d\lambda \frac{\partial P}{\partial \lambda} \quad (1.1.3.2)$$

where  $\lambda$  is the adiabatic parameter (in this case a measure of the atomic displacements) which changes adiabatically from an initial to a final state (centrosymmetric versus fully displaced atoms) while the external field is required to vanish for any value of the parameter. In the second order of perturbation theory, the expression of the integrand in terms of momentum matrix elements becomes:

$$\frac{\partial P}{\partial \lambda} = -i \frac{e\hbar}{\Omega m_e} \sum_k \sum_i^{occ} \sum_j^{empty} \frac{\langle \psi_{ki}^\lambda | \hat{p} | \psi_{kj}^\lambda \rangle \langle \psi_{kj}^\lambda | \partial V_{KS}^\lambda / \partial \lambda | \psi_{ki}^\lambda \rangle}{(\epsilon_{ki}^\lambda - \epsilon_{kj}^\lambda)^2} + c.c. \quad (1.1.3.3)$$

where the sum  $i, j$  over the bands is assumed to include the sum over the spin states, or, in the spin degenerate case there is a factor of 2 in front of the expression. The Kohn-Sham hamiltonian  $V_{KS}$  as well as the eigenvalues and eigenfunctions are lambda dependent which means that they are adiabatically transformed between the two states. Using the  $k$  dependent form of the hamiltonian, the equation above can be rewritten using only the sum over the occupied bands. In order to do this we make use of the following substitutions:

$$\begin{aligned} \langle \psi_{ki}^\lambda | \hat{p} | \psi_{kj}^\lambda \rangle &= \frac{m_e}{\hbar} \langle u_{ki}^\lambda | [\partial / \partial k, \hat{H}(k, \lambda)] | u_{kj}^\lambda \rangle \\ \langle \psi_{kj}^\lambda | \partial V_{KS}^\lambda / \partial \lambda | \psi_{ki}^\lambda \rangle &= \langle u_{ki}^\lambda | [\partial / \partial k, \hat{H}(k, \lambda)] | u_{kj}^\lambda \rangle \end{aligned} \quad (1.1.3.4)$$

Substituting (1.1.3.4) in (1.1.3.3) and making use of the completeness relations, we get Vanderbilt's<sup>6</sup> result of the polarization:

$$\Delta P_\alpha = -|e| \frac{2}{(2\pi)^3} \text{Im} \int_{\text{BZ}} dk \int_0^1 d\lambda \sum_i^{\text{occ}} \left\langle \frac{\partial u_{ki}^\lambda}{\partial k_\alpha} \middle| \frac{\partial u_{ki}^\lambda}{\partial \lambda} \right\rangle \quad (1.1.3.5)$$

where  $\alpha$  is the direction along which we calculate the  $\alpha$  component of the polarization while the perpendicular components are averaged. Looking at this expression it is clear that we are calculating a berry phase that results in calculating the polarization up to a phase factor related with the berry phase quanta. A more detailed expression of the polarization difference that also includes the polarization quanta is given below:

$$\Delta P_\alpha = -i \frac{|e|}{(2\pi)^3} \int_{\text{BZ}} dk \sum_i^{\text{occ}} \left[ \langle u_{ki}^{\lambda=1} | \partial_{k_\alpha} u_{ki}^{\lambda=1} \rangle - \langle u_{ki}^{\lambda=0} | \partial_{k_\alpha} u_{ki}^{\lambda=0} \rangle \right] + \text{int} \times \frac{-|e|}{A} \quad (1.1.3.6)$$

In the above equation, the last term represents the quanta of the polarization where  $\text{int}$  is an integer and  $A$  is the area of the cell perpendicular to the direction  $\alpha$ . The quanta can be interpreted<sup>8</sup> as the number of electrons which were transported across the entire crystal, leaving the crystal invariant and only the fractional part of the expression represents the intrinsic bulk polarization. An even better way to interpret (1.1.3.6) is to cast the expression in terms of centers of Wannier functions that have the form:

$$\langle T_i | \hat{r} | 0_j \rangle = i \frac{\Omega}{(2\pi)^3} \int dk e^{-ikT} \langle u_{ik} | \nabla_k | u_{jk} \rangle \quad (1.1.3.7)$$

where  $T_i$ , an integer multiple of the lattice vector, is set to zero.

With this expression the polarization becomes:

$$\Delta P_\alpha = \frac{-|e|}{\Omega} \sum_i^{\text{occ}} \left[ \langle 0_i | \hat{r} | 0_i \rangle^{\lambda=1} - \langle 0_i | \hat{r} | 0_i \rangle^{\lambda=0} \right] \quad (1.1.3.8)$$

which gives a simple interpretation of the polarization difference as the polarization given by the two point charges localized at the center of the Wannier functions (for initial and

final state) and having the charge equal to the sum of all the electrons belonging to the unit cell. Further, the polarization quanta is seen as an electronic charge localized on the center of an equivalent Wannier function at a position differing by a translation lattice vector.

This robust and elegant theory is called the modern theory of polarization and the results presented in this section were used to calculate the polarization on my work which will be the subject of next chapters.

## ***1.2 Magnetism.***

Before quantum mechanics the problem of magnetism was one of the key dilemmas in physics because, within the picture of classical physics, there was no explanation for why the energy of a magnetic system was affected by an external electric field. The answer comes from quantum mechanics, which associates a half-integer spin to the electron. It is then possible for interacting electrons to have a net magnetic moment in the ground state that will interact with external magnetic fields. In other words, magnetic systems are ones in which the ground state presents a broken symmetry with spin and/or orbital moments of the electrons.

There are two aspects of magnetism depending on whether we are considering the atomic picture or we are dealing with extended system. In open-shell isolated atoms, Hund's rule provides a good description of the spin arrangements by claiming that the electrons will occupy the available states that assure the maximization of the total spin and the orbital momentum. The problem becomes more complicated in a solid where the

long-range magnetic order becomes important. A model that describes the long-range ordering in a solid is the Heisenberg or Ising model<sup>9</sup>. Here we limit our discussion to a qualitative treatment in which the effects of exchange and correlation between the electrons is replaced by an effective field called the Zeeman field  $H_Z$  which is represented in the hamiltonian by  $m(r)V_m(r)$  where  $V_m = \mu H_Z$  and  $m = n^\uparrow - n^\downarrow$ . Introducing this new term in the hamiltonian, it is clear that the energy will have a term coming from the magnetic interaction. We also can write down the equations for magnetization and magnetic susceptibility:

$$m(r) = -\frac{dE}{dV_m(r)} \quad (1.2.1.1)$$

$$\chi(r, r') = -\frac{dm(r)}{dV_m(r')} = \frac{d^2E}{dV_m(r)dV_m(r')} \quad (1.2.1.2)$$

Depending on the curvature of the energy,  $\chi$  can have a minimum at zero magnetization, which will correspond to close-shell atoms with paired spins. However the exchange potential tends to align the spins. This can result in a negative curvature with a maximum at zero magnetization and a minimum at a nonzero value of  $m$ . However, local nonzero magnetization does not assure that the system is ferromagnetic. Depending of the average magnetization there can be an antiferromagnetic arrangement if the average value is zero. At the other extreme, we have a ferromagnetic arrangement when all the spins are collinear and anything in between belong to the class of ferrimagnets.

The reason that magnetism is difficult to treat quantitatively is because real materials are in neither atomic nor band limit and there is a competition between intra-atomic correlation effect and interatomic bond effects. Another challenge rises from spin



orbit coupling which can be ignored for light materials but becomes important for heavy ones, and is known that the calculation of orbital momentum presents real challenges if the symmetry is not the spherical one. An elegant solution for this problem has been perfected within the framework of Density Functional Theory (DFT) and is known as “the frozen spin configuration approach” which is the method implemented in VASP code and used for my calculation of the magnetization.

### 1.3 Methodology and framework

In this section I will present the main equations that describe the dynamics and interactions of the electrons inside a crystal. The framework used to solve the problems subject to next sections is Density Functional Theory<sup>10,11</sup> (DFT), which is a mean field theory and the most widely used theory in predicting the properties of the electronic structure of crystals. This theory will be briefly discussed in the second subsection.

#### 1.3.1 Basic equations for interacting electrons and nuclei

The starting point of the quest of describing the properties of matter is to write down the hamiltonian of the system:

$$\hat{H} = -\frac{\hbar^2}{2m_e} \sum_i \nabla_i^2 + \sum_{i,I} \frac{Z_I e^2}{|r_i - R_I|} + \frac{1}{2} \sum_{i \neq j} \frac{e^2}{|r_i - r_j|} - \sum_I \frac{\hbar^2}{2M_I} \nabla_I^2 + \frac{1}{2} \sum_{I \neq J} \frac{Z_I Z_J e^2}{|R_I - R_J|} \quad (1.3.1.1)$$

where the electrons are lower case subscripts and the nuclei are upper case.  $Z$  and  $M$  are the charge and respectively the mass of the nuclei while  $m_e$  is the mass of the electron. Similarly,  $R$  represents the position of the nuclei and  $r$  the positions of the electrons.

This hamiltonian can be written in a more concise way and the expression obtained represents the fundamental hamiltonian for the theory of electronic structure:

$$\hat{H} = \hat{T} + \hat{V}_{ext} + \hat{V}_{int} + E_{II} \quad (1.3.1.2)$$

where:

$$\begin{aligned} \hat{T} &= -\frac{\hbar^2}{2m_e} \sum_i \nabla_i^2 \\ \hat{V}_{ext} &= \sum_{i,I} \frac{Z_I e^2}{|r_i - R_I|} \\ \hat{V}_{int} &= \frac{1}{2} \sum_{i \neq j} \frac{e^2}{|r_i - r_j|} \end{aligned} \quad (1.3.1.3)$$

Here  $T$  is the kinetic energy operator for the electrons,  $V_{ext}$  is the potential acting on the electrons due to the nuclei,  $V_{int}$  is the operator for electron-electron interaction and  $E_{II}$  is the energy provided by the classical interaction between the nuclei and any other terms that contribute to the total energy without involving any type of electron interaction. Only one term was neglected in (1.3.1.2) compared with (1.3.1.1) and that term is the kinetic energy of the nuclei. The reason for doing this was because this term is much smaller than any of the other terms, and by ignoring it, one gains a great deal of simplification in the problem. By decoupling the electrons and nuclei degrees of freedom one can treat the nuclei in a classical manner while preserving the quantum behavior of the electrons. This approximation is also called the Born-Oppenheimer or adiabatic approximation<sup>12</sup>.

The fundamental equation that governs nonrelativistic quantum mechanics is the Schrödinger equation. Employing the hamiltonian from (1.3.1.2) and writing the time-

independent Schrödinger equation for the many-body system, theoretically we can fully characterize and predict all the properties of the electronic structure of the system in discussion. The equation to be solved is:

$$\widehat{H}|\psi(\{r_i\})\rangle = E|\psi(\{r_i\})\rangle \quad (1.3.1.4)$$

where  $\psi(\{r_i\}) \equiv \psi(r_1, r_2, \dots, r_N)$  is the antisymmetric wavefunction of the electrons with the spin included in the coordinates. After solving (1.3.1.4), the value of any observable in an eigenstate is the expectation value of the operator associated to that particular observable:

$$\langle \widehat{O} \rangle = \frac{\langle \psi | \widehat{O} | \psi \rangle}{\langle \psi | \psi \rangle} \quad (1.3.1.5)$$

The only big challenge here is to solve the Schrödinger equation in (1.3.1.4), but even if we consider the adiabatic approximation, the problem is far from being trivial. Even with the greatest computer resources, in order to be able to tackle some real problems, one has to rely on some good approximations. A very successful approximation is the independent-electron approximation that has two main approaches: the Hartree-Fock<sup>13</sup> approach and the “non-interacting” approach. They are similar in that each takes into consideration the exchange part of the potential but don’t incorporate the correlation effects. In the same time Hartree-Fock approach explicitly includes the electron-electron interaction in the hamiltonian while in the other case the electron-electron interaction is not included directly but rather as part of an effective potential.

A different flavor of a non-interacting approach is Density Functional Theory which is the most widely use theory in electronic structure and the effective potential was

perfected to approximately incorporate the exchange-correlation effects. I will try to give a short summary of this theory in the next section.

### 1.3.2 Density Functional Theory (DFT).

The modern formulation of DFT originated in the famous paper<sup>11</sup> written by P. Hohenberg and W. Kohn in 1964. The foundation is based on two theorems.

**Theorem I:** For any system of interacting particles in an external potential  $V_{ext}(r)$ , the potential  $V_{ext}(r)$  is determined uniquely, except for a constant, by the ground state particle density  $n_0(r)$ .

**Corollary I:** Since the hamiltonian is determined, except for a constant shift in the energy, it follows that the many-body wavefunctions for all states (ground and excited) are determined. *Therefore all properties of the system are completely determined given only the ground state density  $n_0(r)$ .*

A schematic representation of Theorem I is given in *Fig. 1.3.2a*.

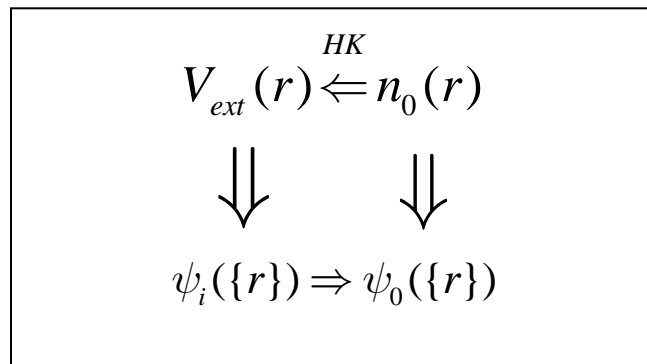


**Fig. 1.3.2a:** Schematic representation of Hohenberg-Khan theorem.

**Theorem II:** A universal functional for the energy  $E[n]$  in terms of the density  $n(r)$  can be defined, valid for any external potential  $V_{ext}(r)$ . For any particular  $V_{ext}(r)$ , the exact ground state energy of the system is the global minimum value of this functional, and the density  $n(r)$  that minimizes the functional is the exact ground state density  $n_0(r)$ .

Even if these theorems are very general, and in principle the ground state density alone is sufficient to determine all the properties of a system, the relation is very subtle and no one has found a way to extract directly from the density any set of properties. The reason that DFT is the most widely used theory today is because of the approach proposed by Kohn and Sham<sup>14</sup> in 1965. Their idea was to replace the difficult interacting many-body system obeying the hamiltonian (1.3.1.1) with a different auxiliary system that can be solved more easily. This idea is also known as Kohn-Sham ansatz and relies on two assumptions:

1. The exact ground state density can be represented by the ground state density of an auxiliary system of non-interacting particles.

2. The auxiliary hamiltonian is chosen to have the usual kinetic operator and an effective local potential  $V_{eff}^\sigma(r)$  acting on an electron of spin  $\sigma$  at point  $r$  and has the form:

$$\hat{H}_{aux}^\sigma = -\frac{1}{2}\nabla^2 + V_{eff}^\sigma(r) \quad (1.3.2.1)$$

The mathematical translation of the Kohn-Sham approach consists in writing down the ground state Kohn-Sham energy functional as follows:

$$E_{KS} = T_s[n] + \int dr V_{ext}(r)n(r) + E_{Hartree}[n] + E_{II} + E_{xc}[n] \quad (1.3.2.2)$$

where  $n(r)$ ,  $T_s[n]$ ,  $V_{ext}(r)$ ,  $E_{Hartree}$ , and  $E_{II}$  are the electron density, independent-particle

kinetic energy, external potential due to nuclei and any other external fields, classical Coulomb interaction energy of the electron density  $n(r)$  and interaction energy of the nuclei, respectively.  $E_{xc}$  is called the exchange-correlation energy and has all the many-body effects due to exchange and correlation effects in it. If the system has  $N$  independent electrons obeying (1.3.2.1), with the ground state having one electron in each of the  $N$  orbitals  $\psi_i(r)$  with the lowest eigenvalues  $\varepsilon_i$  of the Hamiltonian, then one can write expressions for electron density, kinetic energy and Hartree energy as:

$$n(r) = \sum_{\sigma} n(r, \sigma) = \sum_{\sigma} \sum_{i=1}^{N^{\sigma}} |\psi_i^{\sigma}(r)|^2 \quad (1.3.2.3)$$

$$T_s = \frac{1}{2} \sum_{\sigma} \sum_{i=1}^{N^{\sigma}} |\nabla \psi_i^{\sigma}(r)|^2 \quad (1.3.2.4)$$

$$E_{Hartree}[n] = \frac{1}{2} \int d^3r d^3r' \frac{n(r)n(r')}{|r-r'|} \quad (1.3.2.5)$$

In order to get the solution of the auxiliary system for the ground state, we have to minimize the functional (1.3.2.2) with respect to the density. This will lead us to the Kohn-Sham Schrödinger-like equation:

$$\left( H_{KS}^{\sigma} - \varepsilon_i^{\sigma} \right) \psi_i^{\sigma}(r) = 0 \quad (1.3.2.6)$$

with

$$\widehat{H}_{KS}^{\sigma}(r) = -\frac{1}{2} \nabla^2 + V_{KS}^{\sigma}(r) \quad (1.3.2.7)$$

$$V_{KS}^{\sigma}(r) = V_{ext}(r) + \frac{\delta E_{Hartree}}{\delta n(r, \sigma)} + \frac{\delta E_{xc}}{\delta n(r, \sigma)} = V_{ext}(r) + V_{Hartree}(r) + V_{xc}^{\sigma}(r) \quad (1.3.2.8)$$

Equations (1.3.2.6) - (1.3.2.8) are the well known Kohn-Sham equation.

The equations have the form of independent-particle equations with a potential that must be found self-consistently with the resulting density. These equations are independent of any approximations to the function  $E_{xc}[n]$ , and would lead to the exact ground state density and energy for the interacting system, if the exact functional  $E_{xc}[n]$  were known. The Kohn-Sham equations have to be solved self-consistently since  $V_{Hartree}$  and  $V_{xc}$  depend explicitly on the charge density  $n(r)$ , given by the eigenstates  $\psi_i$ , which in turn are determined by these potentials. In order to turn this into practice, an initial guess, e.g. a superposition of atomic charges, is used. On the basis of (1.3.2.6), the new charge density is obtained by summing over the occupied Kohn-Sham orbitals  $\psi_i$ . Afterwards, the Hartree and exchange-correlation potentials are then constructed. This process has to be repeated until convergence is reached. In practice the new charge density is mixed with the previous one in order to avoid numerical instabilities. *Fig. 1.3.2b* gives a schematic overview of the iterative algorithm.

After the charge density convergence (or the energy convergence) is reached, the next step is to calculate the forces using Hellmann-Feynman theorem<sup>15,16</sup> and move the ions accordingly towards the equilibrium position. Each time the ions are moved, the self-consistent calculation for finding the new density related with the new atomic configuration is performed. The ions are moved until the calculated forces are considered small enough and, at this point, the system is considered at the geometrical equilibrium. At this stage all the important properties can be derived from the equilibrium energy and density.

The whole picture is almost complete with the exception of one important ingredient which is the form of exchange-correlation functional from where one can

derive the exchange-correlation potential. Even though the exact exchange-correlation functional must be very complex, great progress has been made with remarkably simple approximations. The two most simple and popular approximations are the local density approximation<sup>16</sup> (LDA) and generalized gradient approximation<sup>17,18</sup> (GGA).

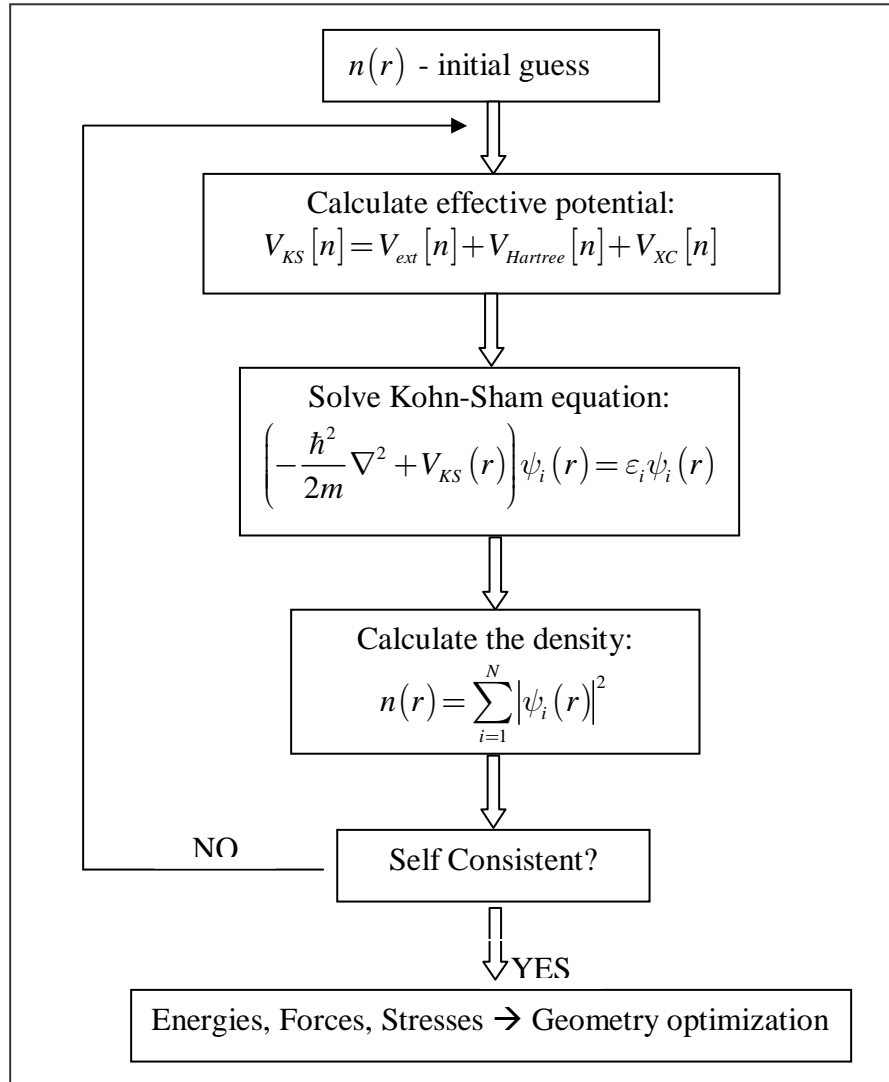


**Fig. 1.3.2b: Flowchart of self-consistent Kohn-Sham calculation.**



In summary, in the current section I showed some of the main equations that govern the electronic interaction in matter and also gave an overview of the density functional theory (DFT) which will be the framework for the problems discussed on the next chapters.

## Chapter 2 The effect of pressure on GeTe

Ferroelectric crystals find a multiplicity of technological functions; their pyroelectric nature is used in thermal and infrared sensors. In BaTiO<sub>3</sub> and some other ferroelectrics, light induces changes in the refracting indices, which is used for information storage and real-time optical processors. Their high dielectric constants make them candidates to replace SiO<sub>2</sub> in metal-oxide-semiconductor devices. Those that are piezoelectrics find numerous applications in electromechanical transducers. Some can be used for reversible phase change optical data storage. For example, stoichiometric films of GeTe can be crystallized with laser pulses of less than 100 ns duration<sup>25</sup>.

Having only two atoms per unit cell, GeTe is undoubtedly the simplest ferroelectric. Above about 720 K it crystallizes in the rock salt structure<sup>26</sup>, as do many of the other IV-VI compounds such as PbTe, SnTe, PbSe, etc. It is the only one (at about 720 K) to undergo a displacive transition to a trigonal (rhombohedral) structure consisting of an inner displacement along a [111] direction with a corresponding [111] stretch of the lattice. Using a model Hamiltonian with parameters obtained from self consistent density functional calculations, Rabe and Joannopoulos<sup>27</sup> predicted a transition temperature of  $657 \pm 100$  K. There is a long history of the pressure induced phase transition at room temperature but no calculations of the critical pressure of which we are aware. The experimental value is extremely sensitive to any shear component in the applied pressure<sup>29</sup>. Kabalkina et al<sup>30</sup> obtained a 3.5 GPa critical pressure accompanied by a sudden 3% decrease in volume. Using silicone grease, a non-hydrostatic pressure transmitting medium, Leger and Redon<sup>28</sup> obtained a transition around 4 GPa with no

volume discontinuity. Using a liquid 4:1 methanol-ethanol medium they found the rhombohedral phase persisted up to 8 GPa, the maximum investigated pressure. Nevertheless, Onodera *et al.*<sup>31</sup> find that the transition occurs at 3 GPa (with no volume discontinuity).

A simple physical picture for the restoration of the rock salt structure under pressure is as follows. The sublattice displacements shorten three of the six nearest neighbor bonds while lengthening the other three. Under pressure the long bonds are easily compressed while the short bonds are not. As the pressure is increased and the bond lengths become more equal, at some point it becomes energetically favorable to go to complete equality and for the trigonal distortion, which was driven by the sublattice displacements, to vanish. A somewhat different explanation was given by Kornev *et al.*<sup>32</sup>. They say that ferroelectricity results from a delicate balance between long range Coulomb ionic interactions favoring ferroelectric distortions and short range electronic effects preferring the undistorted paraelectric cubic structure and that the balance can be tipped towards ferroelectricity by small covalent effects.

## 2.1 Computational details

Because there is some evidence that the energy gap of GeTe has a relatively strong dependence on spin-orbit coupling<sup>33</sup>, we have performed fully relativistic calculations of the electronic structure of GeTe using the projected augmented wave method<sup>34</sup> (PAW) as implemented in the VASP software package<sup>35</sup>. The exchange-correlation density functional was calculated in both the local density approximation

(LDA) and the PBE<sup>24</sup> form of the generalized gradient approximation (GGA). A 20 x 20 x 20 k-point mesh was used in the Brillouin zone (BZ) which was integrated over using the quadratic tetrahedron scheme<sup>35</sup>. We expanded in all plane waves with energy below 21 Ry and reduced the force on the displaced sublattices to less than 1.5 meV/Å. Our convergence at the LDA equilibrium volume is displayed in *Table 2.1.1*.

<b>k - mesh</b>	<b>pw (Ry)</b>	<b>meV/Å</b>	<b>E<sub>c</sub> (eV)</b>	<b>Δ E<sub>c</sub>(meV)</b>
20x20x20	21	1.5	7.769030	
20x20x20	21	0.3	7.769089	0.059
20x20x20	32	0.3	7.769382	0.293
26x26x26	32	0.3	7.769509	0.127

*Table 2.1.1: Convergence parameters and the effect on the energy.*

We reduced the force criterion<sup>36</sup> from 1.5 meV/Å to 0.3 meV/Å, which increased the cohesive energy by 0.059 meV. Because we are interested in the energy differences between the cubic and trigonal structures and there are no forces in the cubic case, as well as the fact that the other convergence properties are expected to be similar for the two structures, this 0.059 meV may be more significant than the 0.293 meV gained by increasing the plane wave cutoff energy from 21 Ry to 32 Ry. The increase of 0.127 meV on increasing the k point sampling from 20 x 20 x 20 to 26 x 26 x 26 may also be similar in the trigonal and cubic cases.

## 2.2 Discussion of the results

In *Table 2.2.1* are listed all the important results of our calculations. After discussing these we will go into somewhat more detail for the LDA case (the GGA is similar and yields no additional physics) using the data in *Table 2.2.2*.

	$\Omega(\text{\AA}^3)$	$a(\text{\AA})$	$\alpha(^{\circ})$	$E_{\text{coh}}(\text{eV})$	$B(\text{GPa})$	$\tau(a)$	$E_{\text{gap}}(\text{meV})$	$P(\mu\text{Ccm}^{-2})$	$p_c(\text{GPa})$
<b>LDA</b>	50.96	5.886	89.24	7.77	37.64	0.0217	209	61.13	5.313
<b>GGA</b>	55.96	6.074	88.06	6.46	32.70	0.0304	469	64.90	8.448
<b>exp</b>	53.31 <sup>a</sup>	5.98 <sup>a</sup>	88.35 <sup>a</sup>	-	49.9 <sup>b</sup>	0.0248 <sup>a</sup>	200 <sup>c</sup>	-	3 <sup>b</sup>
<b>exp<sup>d</sup></b>	-	5.986	88.59	-	< 38.3	-	-	-	> 8

<sup>a</sup>Reference 29

<sup>b</sup>Reference 31

<sup>c</sup>Reference 42

<sup>d</sup>Reference 28

**Table 2.2.1: Comparison of LDA and GGA trigonal GeTe results with experiment.**

The first column compares the rhombohedral unit cell volumes, which are smaller (LDA) and larger (GGA) than experiment. The larger discrepancy with experiment (LDA) of the “cubic” lattice constants is less than 2%. Experimental papers do not as a rule give a value for the trigonal lattice constant<sup>38</sup>. The second column compares the angle between two “cubic” lattice vectors. Again, the LDA and GGA results are on opposite sides of the experimental values. There are no experimental values for the GeTe cohesive energy but comparing with the sum of the Ge and Te cohesive energies<sup>8</sup> (6.04 eV) we see that our calculated values<sup>39</sup> indicate that GeTe is stable against phase separation.. The bulk moduli in the fifth column were obtained from a three point fit. A five point Vinet<sup>40</sup> fit for the LDA (GGA) case yields 34.908 GPa (33.216 GPa) while an

eleven point fit yields 43.436 GPa (30.024 GPa) closely bracketing the three point GGA result and also bracketing the LDA result, but not so closely. It has been our<sup>41</sup> experience that discrepancies within an equation of state (EOS) due to fitting at different numbers of points are much larger than discrepancies between different EOS. The less than 38.36 GPa quoted from Ref. 27 is deduced from the statement that the GeTe bulk modulus is less than that of<sup>42</sup> Sb. The sixth column lists the deviation of the separation of the Ge and Te sublattices away from  $0.5a$ . The LDA and GGA results are close to and on opposite sides of the experimental value. The seventh column lists the indirect energy gap, which is between the L point and the point at (0.35, 0.2, 0.2) along the trigonal reciprocal lattice vectors for both LDA and GGA. Ignoring the small trigonal distortion, this would be the (0.05, 0.35, 0.35) point in the fcc BZ. The LDA gap is in near perfect agreement with the value of 200 meV obtained from tunneling spectroscopy<sup>43</sup>. The GGA gap is much too large; it appears that the gap is very strongly coupled to the deviation of  $\alpha$  from  $90^\circ$ . Note that the GGA/LDA gap ratio is 2.55. Although this gap discrepancy could be attributed to the larger GGA equilibrium volume, note that (in *Table 2.2.2*) the rock salt structure has a gap of only 1.8 meV at the trigonal equilibrium volume. The direct gap at L is 369 meV (LDA) and 685 meV (GGA). The direct gap at Z, which would be the fourth L point in the fcc BZ, is even wider: 429 meV for LDA and 1054 meV for GGA. The LDA energy bands on the reflection plane are displayed in *Fig.2.2.1*. The notation of Slater<sup>44</sup> is used for the symmetry points except for U, the point at which the rectangular and hexagonal faces of the BZ meet, because it has no symmetry beyond the reflection. It corresponds to the fcc U point.

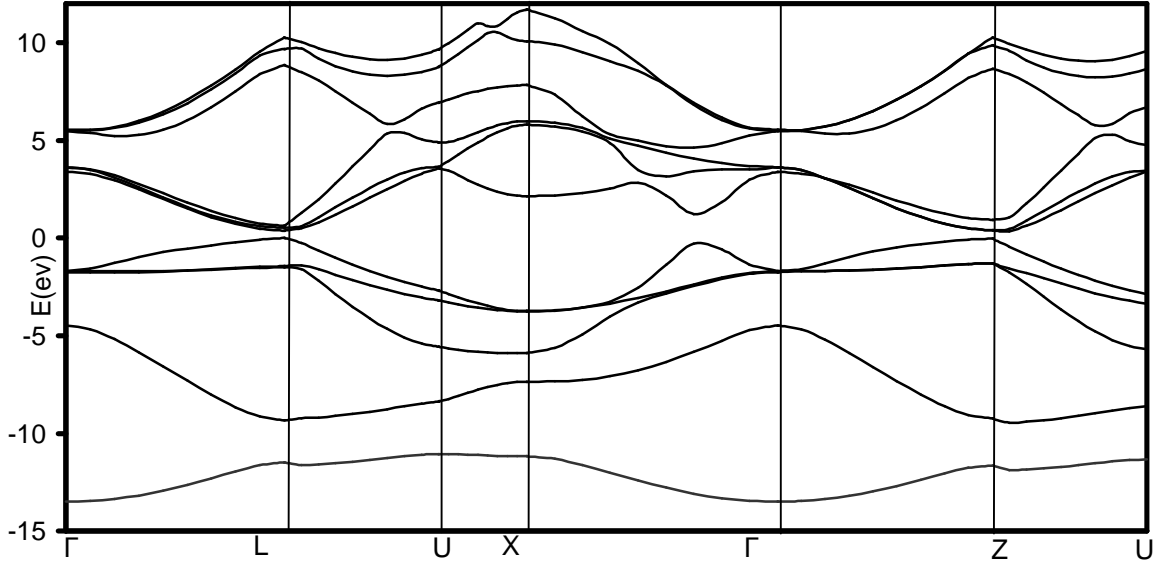


*Fig. 2.2.1: Energy bands of rhombohedral GeTe.*

Using the Berry phase formula for the zero electric field polarization<sup>11</sup> as implemented in VASP<sup>34</sup>, we obtained the values listed in the seventh column. For the LDA,  $\mathbf{P} = 61.13 \mu\text{Ccm}^{-2}$ . The Berry phase calculation of the polarization has an uncertainty of

$$\Delta\mathbf{P} = (2e/\Omega) \sum_{n=1}^5 \mathbf{R}_n$$

where the sum is over the energy bands and  $\mathbf{R}_n$  is a lattice vector in the direction of the polarization. Taking one of the  $\mathbf{R}_n$  to be the shortest (111) lattice vector and the rest to be zero, we obtain a minimum LDA  $\Delta\mathbf{P}$  of  $648 \mu\text{Ccm}^{-2}$ . This represents the translation of one band of electrons through  $\mathbf{R}_n$  and results in the next to smallest LDA value of  $\mathbf{P}$  being  $-587 \mu\text{Ccm}^{-2}$ , which is clearly unphysical. It is surprising that the LDA and GGA yield

such similar results, considering their large difference in  $(90^\circ-\alpha)$  and in the sublattice displacement  $\tau$ . There are no experimental values for GeTe but our calculated values are surprisingly large, agreeing very well with the largest experimental values found in other displacive ferroelectrics such as<sup>8</sup> LiTaO<sub>3</sub> (50  $\mu\text{Ccm}^{-2}$ ), PbTiO<sub>3</sub> ( $>50 \mu\text{Ccm}^{-2}$ ), and LiNbO<sub>3</sub> (71  $\mu\text{Ccm}^{-2}$ ).

The Born effective charge<sup>47, 48</sup>  $Z^*$  is obtained from  $Z^*e = \Omega(\Delta P/\Delta\tau)$ . We took  $\Delta\tau$  to be  $0.1\tau$  and calculated the polarization with  $\tau$  replaced by  $0.9\tau$ , keeping the lattice constants fixed. The numerical values needed to evaluate  $Z^*$  are given in *Table 2.2.3*.  $P_{\text{xtrp}}$  is the polarization extrapolated from  $0.9\tau$  to  $\tau$ ,  $P_{\text{xtrp}} = P(0.9\tau)/0.9$ . The ratio  $P_{\text{xtrp}}/P(\tau)$  is also listed to demonstrate the nonlinearity of  $P$  with  $\tau$ . The large values of  $Z^*$  were to be expected because of the large values of the polarization, which are sufficient, but not necessary, to obtain large  $Z^*$ 's<sup>49</sup>. There are no experimental values but if one makes the geometric extrapolation  $8.1/6.5 = P/8.1$  where 8.1 and 6.5 are the experimental<sup>47</sup> values for PbTe and SnTe, one obtains  $Z^* = 10.09$ , in remarkable agreement with our LDA result. Tanaka and Shindo<sup>47</sup> obtained  $Z^* = 7.7$  from an empirical pseudopotential calculation.

	<b>P(<math>\tau</math>)</b>	<b>P (0.9<math>\tau</math>)</b>	<b><math>\Delta P</math></b>	<b><math>\Delta\tau</math> (Å)</b>	<b><math>Z^*</math></b>	<b><math>P_{\text{xtrp}}/P(\tau)</math></b>
<b>LDA</b>	61.13	57.07	4.06	0.0127	10.11	1.037
<b>GGA</b>	64.90	59.46	5.44	0.0185	10.25	1.018

***Table 2.2.3: Polarization effective charge  $Z^*$ .***



Further insight into the reason for the large value of  $Z^*$  may be obtained from plots of the pseudocharge density along the nearest neighbor direction in *Fig.2.2.2* and along the 3-fold axis in *Fig.2.2.3*.

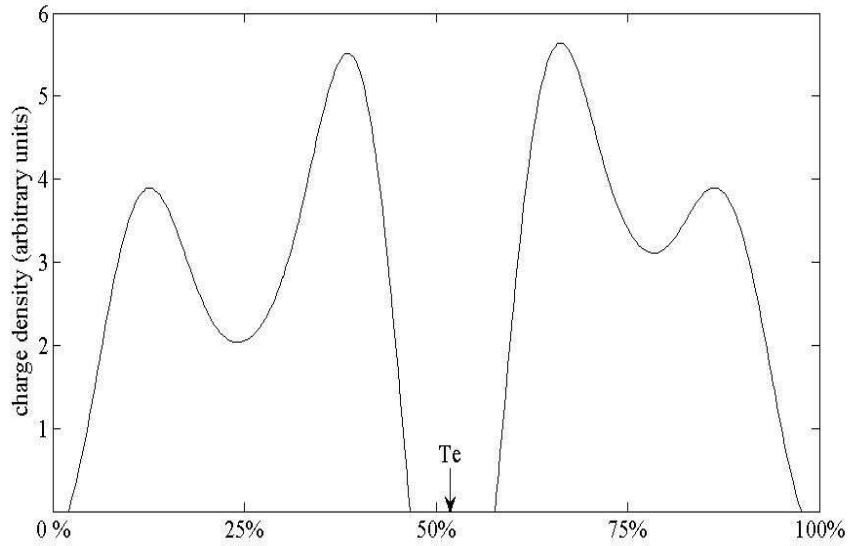


***Fig. 2.2.2: Plot of the pseudocharge density along the nearest neighbor direction in trigonal GeTe.***

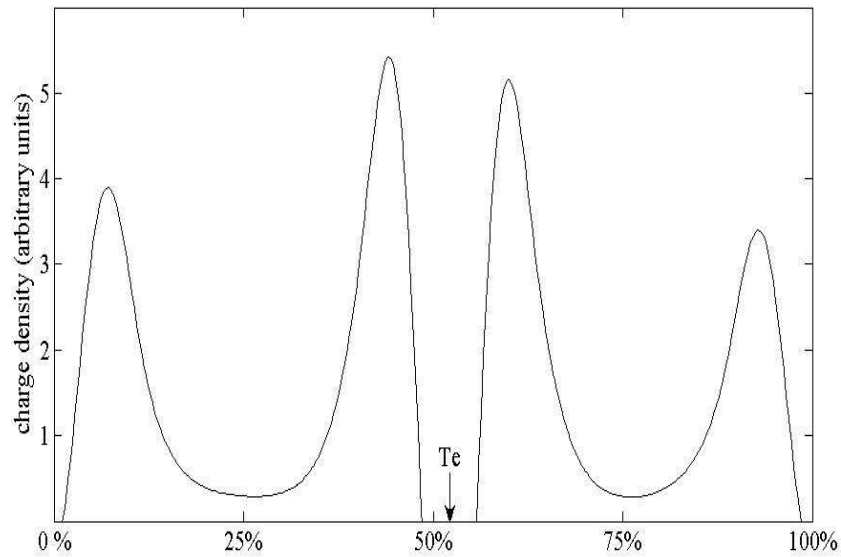


**Fig. 2.2.3: Identical to Fig. 2.2.2 except that the plot is along the 3-fold axis.**

In Fig.2.2.2 we see extremely strong covalent bonding and the shorter bond is stronger (i.e. it has a shallower minimum in the bond) than the longer bond, which was to be expected. The plot along the 3-fold axis is much more interesting. Extrapolating from this one dimensional picture to three dimensions, we note that both atoms are polarized with their larger charge density peaks on the long bond side of the atoms. This means that rather than moving with the ions and screening out a part of their contribution, the electrons move in the opposite direction and add to both the polarization and  $Z^*$ . The calculated transition pressures in the last column of *Table2.2.1* lie within the large range of experimental values. This large difference between the experimental results could be due to different sample stoichiometries. We note that the sample used in Ref. 43 had  $2 \times 10^{20}$  holes per  $\text{cm}^3$ , indicating a similar density of vacancies or impurities.

	$\Omega(\text{\AA}^3)$	$a(\text{\AA})$	$\alpha(^{\circ})$	$\tau(a)$	$E_c^{\text{trig}}(\text{eV})$	$E_c^{\text{cube}}(\text{eV})$	$\Delta E(\text{meV})$	$E_g^{\text{trig}}(\text{meV})$	$E_g^{\text{cube}}(\text{meV})$	$p(\text{GPa})$
<b>5%</b>	53.5080	5.9830	88.55	0.027434	7.75594	7.72754	28.395	411.7	205.3	
<b>4%</b>	52.9984	5.9636	88.74	0.025900	7.76113	7.73674	24.390	379.2	175.5	-1.270
<b>3%</b>	52.4888	5.9443	88.86	0.024764	7.76523	7.74449	20.747	340.2	144.7	-0.841
<b>2%</b>	51.9792	5.9248	88.97	0.023500	7.76716	7.75067	16.489	311.8	112.8	-0.609
<b>1%</b>	51.4696	5.9053	89.11	0.022132	7.76791	7.75524	12.663	282.2	80.0	-0.320
<b>0%</b>	50.9601	5.8856	89.24	0.021681	7.76903	7.75907	9.966	208.7	1.8	0.009
<b>-1%</b>	50.4504	5.8657	89.35	0.019422	7.76793	7.75909	8.846	195.1	11.4	0.593
<b>-2%</b>	49.9408	5.8459	89.41	0.018097	7.76572	7.75821	7.511	174.2	24.5	1.158
<b>-3%</b>	49.4312	5.8260	89.43	0.016606	7.75969	7.75424	5.450	138.8	61.1	1.754
<b>-4%</b>	48.9216	5.8058	89.58	0.015245	7.75454	7.74940	5.137	79.4	45.6	2.371
<b>-5%</b>	48.4120	5.7855	89.64	0.013681	7.74524	7.74231	2.928	43.1	12.4	3.012
<b>-6%</b>	47.9024	5.7651	89.71	0.012195	7.73478	7.73298	1.807	35.3	-11.5	3.684
<b>-7%</b>	47.3928	5.7446	89.78	0.010536	7.72209	7.72115	0.938	28.4	-18.3	4.394
<b>-8%</b>	46.8832	5.7239	89.85	0.008513	7.70706	7.70678	0.284	11.0	-42.3	5.141
<b>-9%</b>	46.3736	5.7031	89.94	0.004216	7.68963	7.68972	-0.094	-76.0	-80.5	5.923
<b>-10%</b>	45.8640	5.6822	89.96	0.000653	7.66971	7.66979	-0.076	-95.0	-119.5	6.742
<b>-11%</b>	45.3544	5.6610	89.98	0.000470	7.64673	7.64680	-0.071	-163.0	-159.5	7.614
<b>-12%</b>	44.8448	5.6397	89.97	0.000201	7.62055	7.62064	-0.082	-196.6	-200.6	8.575
<b>-13%</b>	44.3352	5.6183	89.96	0.000077	7.59292	7.59296	-0.042	-240.2	-241.5	9.672
<b>-14%</b>	43.8256	5.5967	89.95	0.000030	7.55982	7.55988	-0.059	-279.1	-281.8	10.940
<b>-15%</b>	43.3160	5.5749	89.95	0.000013	7.52279	7.52283	-0.035	-330.5	-332.6	12.340
<b>-16%</b>	42.8064	5.5529	89.96	0.000004	7.48180	7.48184	-0.045	-396.6	-398.2	

**Table 2.2.2: Trigonal and cubic GeTe quantities as a function of applied pressure.**

*Fig.2.2.4* is a plot of the LDA cohesive energy of the trigonal and rock salt structures as a function of unit cell volume whose values are listed in *Table2.2.2*. Note that the curves in *Fig.2.2.4* represent the raw data with no smoothing. The trigonal curve is less smooth than the rock salt because for a fixed volume the trigonal energy must be minimized with respect to  $\alpha$  and  $\tau$  whereas the rock salt energy has no parameter

dependence. As far as one can tell from *Fig.2.2.4* the transition is second order, in agreement with Onodera et al.<sup>31</sup>

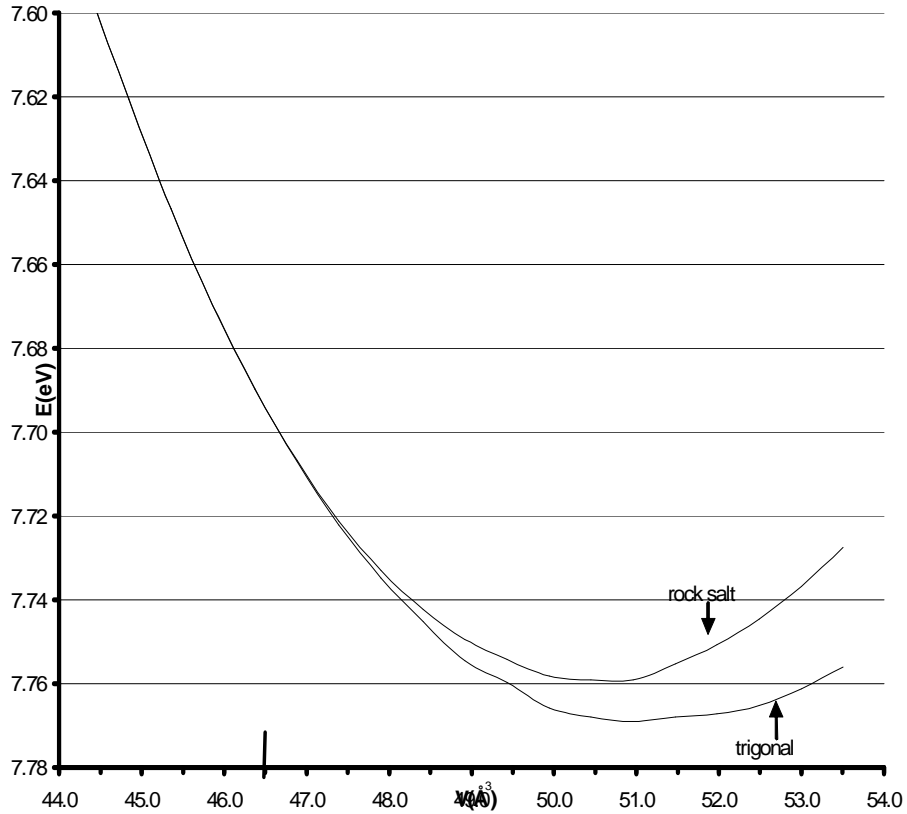


**Fig. 2.2.4: Cohesive energy vs. volume plots for rock salt and rhombohedral GeTe.**

We note that the transition occurs just after the trigonal indirect energy gap becomes negative i.e. just after trigonal GeTe becomes a semimetal. The same is true for the GGA calculation even though it occurs at a considerably higher pressure. This leads us to believe that this is cause and effect rather than coincidence. Of course, because of screening by the conduction electrons, a metal cannot be ferroelectric. However, there is no reason that GeTe could not have become paraelectric well before the energy gap

closed. The difference in those cohesive energies is also the difference between the total energies and therefore (according to *Table 2.2.2*) at a unit cell volume of about  $46.50 \text{ \AA}^3$  (a reduction of 8.75% of the equilibrium volume), where the cohesive energy curves cross, is a first estimate for the point where the phase transition occurs. Our conclusion would be different if the 0.059 meV increase in the trigonal cohesive energy with the more stringent force criterion at the equilibrium volume were to apply at the transition volume. We used the same stringent criterion at the 9% volume reduction and found a trigonal cohesive energy increase of only 0.002 meV. VASP allows one to pick a force criterion and the code then picks a commensurate stress criterion. The former seems satisfactory as  $\tau(a)$  converges to 0.0 but the latter does not, as  $\alpha$  does not converge to  $90^\circ$ . To get the critical pressure we fit  $E_c^{\text{trig}}$  with a ninth order spline and obtained 5.65 GPa at the 8.75% reduction in unit cell volume. After fitting  $E_c^{\text{cube}}$ , the ninth order spline resulted in an 8.32% reduction in volume at the cubic and trigonal energy spline curves' crossover point at which point the critical pressure was 5.42 GPa. The difference between these two critical pressures can be taken as an estimate of the uncertainty in our results. The latter results are listed in *Table 2.2.4* with a 'o' subscript for comparison with the enthalpy minimization results. A Vinet<sup>41</sup> fit resulted in a 14.81% volume reduction at the crossover point and a 9.71 GPa critical pressure and thus was not further considered<sup>50</sup>.

	H(eV)	$p_c$ (GPa)	$V_{\text{trig}}(\text{\AA}^3)$	$V_{\text{cube}}(\text{\AA}^3)$	$\Delta V(\text{\AA}^3)$	E(eV)	$p_{co}$ (GPa)	$V_{co}(\text{\AA}^3)$
LDA	-6.1601	5.313	46.7582	46.6683	0.0899	7.7005	5.417	46.7201
GGA	-3.7559	8.448	47.6777	47.6138	0.0639	6.2761	8.523	47.6568

***Table 2.2.4: Comparison of enthalpy vs. energy based critical parameters.***

To calculate  $H = E + pV$ , for both the cubic and trigonal phases, we took their  $E(V)$  fits and derivatives of the fits,  $p$ , to obtain  $H(p)$  at the 22 volumes listed in *Table 2.2.2*. These  $H(p)$  were fit with the nine point spline. The pressure at which the two spline curves cross is the critical pressure which is listed in *Table 2.2.4* along with the cubic and trigonal volumes at the critical pressure. The results differ only slightly, and in the direction expected, from those obtained from equating the energies. The transition is first order, but only barely, with a volume discontinuity of 0.19%. Note also that  $V_{\text{trig}} > V_0 > V_{\text{cube}}$ , as expected. The critical pressure of 5.313 GPa is only 0.104 GPa less than  $p_{\text{co}}$  which is much less than the uncertainty previously discussed. The GGA volume discontinuity is only 0.134% and the critical pressure only 0.075 GPa below  $p_{\text{co}}$ .

### 2.3 Conclusion

To recapitulate, using both the LDA and GGA, we calculated many of the ground state properties of rhombohedral GeTe. Except for the energy gap where the LDA was in near perfect agreement with experiment, the LDA and GGA results were on opposite sides of the experimental values. There are no experimental values for the polarization where the LDA and GGA results were unexpectedly large, but in good agreement with each other and with other ferroelectrics. From the polarization we obtained the Born effective charge which was correspondingly large. We then calculated most of these properties as a function of volume as well as some for the rock salt structure to find the volume and pressure at which the trigonal to rock salt transition occurs. We found that for both LDA and GGA the phase transition is first order, but with a volume discontinuity

that may be too small to measure, and that it occurred at a pressure close to that at which the energy gap vanishes.

## Chapter 3 DFT study of multiferroic $\text{Bi}_2\text{NiMnO}_6$

Ferromagnetic ferroelectric multiferroic materials appear to have great potential for device applications. If the magnetization  $M$  and the electric polarization  $P$  are uncoupled, they can be used to encode four different logic states. For example, Gajek *et al.*<sup>5</sup> have reported using 2 nm thick films of  $\text{La}_{0.1}\text{Bi}_{0.9}\text{MnO}_3$  as spin filtering tunnel barriers, the magnetization and electric polarization of which can be switched independently, giving rise to four different resistance states. There has been much effort expended to find strongly coupled systems. There has been some success in inducing a reversal of the electric polarization<sup>48, 49</sup> with a magnetic field but thus far, as far as we know, only suggestions<sup>50</sup> exist for reversing the magnetization with an electric field. Fennie and Rabe<sup>51</sup> have demonstrated theoretically that epitaxially strained  $\text{EuTiO}_3$  can be switched from its antiferromagnetic-paraelectric phase to a ferromagnetic-ferroelectric phase with the application of either an electric or magnetic field, but that the direction of the magnetization cannot be reversed in this case by an electric field.

There exist relatively few magnetoelectric multiferroics, and most of those are antiferromagnetic. They form a fascinating field of study which can be framed by two questions asked by Nicola Spaldin (nee Hill)<sup>1-4</sup>, “Why are there so few magnetic ferroelectrics?” and “Why are there any magnetic ferroelectrics?” Covalent bonding between the transition metal (TM)  $d$ - and the oxygen  $2p$ -electrons in the ferroelectric perovskites destroys any possibility of magnetism and seems to be essential for stabilizing the ferroelectric distortion<sup>1</sup>. There does not seem to be any disagreement with this explanation but our interpretation of the nature of the covalent bond and how it



suppresses magnetism<sup>52</sup> differs from that of Spaldin. Seshadri and Hill<sup>3</sup> argued that the large distortion in multiferroic BiMnO<sub>3</sub> is not due to TM-O bonding but rather due to the Bi moving away from a site with inversion symmetry in order to allow its 6s and 6p electrons to hybridize with each other. This idea actually had been proposed<sup>53</sup> as long ago as 1968. Somewhat later, Hill and Filippetti<sup>2</sup> noted that tight binding calculations indicate that it is Bi-O covalency that drives the distortion, but they<sup>2, 54</sup> still suggested that it is the stereochemical activity of the Bi 6s<sup>2</sup> lone pair that causes the structural distortion. Shishidou *et al.*<sup>55</sup> pointed out that the Bi 6s states can hardly play any positive role since they are fully occupied and at a very deep binding energy. They attributed the distortion to strong hybridization between Bi 6p and O 2p states. Other explanations have been given<sup>2, 56</sup> for YMnO<sub>3</sub>, a prototypical hexagonal antiferromagnetic ferroelectric rare earth manganite, but we shall limit our further discussion to the distorted ferromagnetic perovskites.

Very recently Belik *et al.*<sup>57</sup>, using selected area and convergent beam electron diffraction, found that bulk BiMnO<sub>3</sub> crystallizes in the centrosymmetric space group C2c. This, if correct, overturns the many previous results<sup>58</sup> that found the structural phase transition at T<sub>E</sub> ~ 770 K was to the non-centrosymmetric C2 structure<sup>59</sup>. They suggested that measured dielectric hysteresis loops were due to nonlinear dielectric losses rather than ferroelectricity and that the observation of reflections characteristic of the C2 space group were due to double diffraction. They also considered it possible that impurities or poor stoichiometry could cause BiMnO<sub>3</sub> to crystallize in the C2 space group. They found a magnetization of 3.92 μ<sub>B</sub> per formula unit at 5K with a 5 T field but almost no remnant magnetization and a Curie temperature of ~100 K. An LSDA calculation<sup>54</sup> found

BiMnO<sub>3</sub> to be a metal, but with a Hubbard U – J of 6.94 eV a gap opened up and a Berry phase<sup>11</sup> calculation yielded  $P = 0.52 \mu\text{C cm}^{-2}$ , an order of magnitude larger than the experimental values. Among the handful of other ferromagnetic ferroelectrics BiFeO<sub>3</sub> may be the most interesting, both because of its high transition temperatures and its thin film properties<sup>60</sup> Bulk samples become antiferromagnetic (with a very small ferromagnetic component due to spin canting) at  $T_N \sim 643 \text{ K}$  and ferroelectric at  $T_E \sim 1103 \text{ K}$  with a spontaneous polarization of  $6.1 \mu\text{C cm}^{-2}$  at 77 K. In a thin film a remnant polarization of 50 to 60  $\mu\text{C cm}^{-2}$  was obtained. A saturation magnetization of  $\sim 1 \mu_B$  per unit cell was obtained with a 70 nm film (with a negligible remnant magnetization). The saturation magnetization was very dependent on film thickness, dropping to  $\sim 0.03 \mu_B$  in a 400 nm film. Yun *et al.*<sup>61</sup> reported remnant polarizations of  $100 \mu\text{C cm}^{-2}$  at room temperature and  $146 \mu\text{C cm}^{-2}$  at 90 K in 300 nm films. The thin film has a tetragonal structure while bulk BiFeO<sub>3</sub> is rhombohedral. Interestingly, Neaton *et al.*<sup>62</sup> performed LSDA+U Berry phase calculations for the bulk structure and obtained thin film like polarizations of 90-100  $\mu\text{C/cm}^2$ , depending on the parameter U.

Recently Bi<sub>2</sub>NiMnO<sub>6</sub> has been synthesized<sup>63</sup> as a heavily distorted double perovskite with four formula units in a monoclinic unit cell as shown in Fig. 1. The magnetization measured at 5 K was  $4.1 \mu_B$  per formula unit at 5 T. That this was less than  $5 \mu_B$  was attributed to a small amount of Ni-Mn antisite disorder. The residual magnetization, if any, was too small to be discernable in their Figure 3. Unfortunately,  $T_M = 140 \text{ K}$ , well below room temperature, making it unlikely that Bi<sub>2</sub>NiMnO<sub>6</sub> will have any practical applications, while  $T_E = 485 \text{ K}$  is fairly low but still well above room temperature. A very recent thin film measurement<sup>64</sup> yielded a saturated magnetization of

4.5  $\mu_B$  and a saturated polarization of about 5  $\mu C/cm^2$  at 7 K. The only calculation<sup>65</sup> of which we are aware assumed a cubic double perovskite structure with an 8 Å lattice constant for this highly distorted crystal, so that the comparison we shall make with their results is not expected to result in agreement. We have performed electronic structure calculations for  $Bi_2NiMnO_6$  using both the GGA and GGA+U density functionals. In the next section we describe our computational method and discuss the crystal symmetry, which will give insight into the nature of the electric polarization. In the third section our results are given and compared with experiment.

### *3.1 Computational Method and Crystal Symmetry.*

Density functional calculations were performed using the projected augmented wave<sup>34</sup> method (PAW) as implemented in the VASP code<sup>35</sup>. The PBE form<sup>24</sup> of the generalized gradient approximation was used, both without and with a Hubbard U. We took  $(U-J)_{Mn} = 3.5$  eV and  $(U-J)_{Ni} = 4.0$  eV, assuming that values used elsewhere<sup>66, 67</sup> to obtain agreement with experiment are transportable to this situation<sup>68</sup>. Because Bi plays an important role in multiferroics and it is the heaviest non-radioactive atom, we thought it appropriate to include the spin-orbit interaction and since the orientation of  $\mathbf{M}$  relative to  $\mathbf{P}$  is of interest, we allowed the magnetization to be non-collinear. Because we were already using spinor wave functions, this incurred very little extra computational cost. Unfortunately, this precludes us from making orbital projections of the density of states (DOS) but does allow projections of the charge and Cartesian components of the

magnetization within inscribed spheres. From a Curie-Weiss fit to the magnetic susceptibility, an effective Mn moment of 4.69 (4.79)  $\mu_B$  at low (high) temperature was obtained<sup>57</sup> for BiMnO<sub>3</sub> although the measured magnetization was 3.92  $\mu_B$  per formula unit. If the atomic moments obtained from Curie-Weiss are meaningful, they must be noncollinear, which gives an additional rationale for allowing for noncollinearity in Bi<sub>2</sub>NiMnO<sub>6</sub>. In order not to prejudice the magnitude or direction of  $\mathbf{M}$ , we started with the magnetization on the four Mn in the (001), (00-1), (010), and (0-10) directions with magnitude 3 or 5  $\mu_B$ . The other atoms (including Ni) were given polarizations of (0,0,0.01) and (0,0,-0.01)  $\mu_B$ . A 4 $\times$ 8 $\times$ 4  $\mathbf{k}$ -point sample of the Brillouin zone was used. The Bi 5*d* and Mn 3*p* outer core electrons were treated as valence electrons. The basis sets contained all plane waves up to 18.9 Ry. The atomic forces were reduced to less than 10 meV/Å or, equivalently, until the total energy was converged to 10<sup>-6</sup> eV per 40 atom unit cell.

*Fig.3.1.1* is the monoclinic unit cell containing four formula units of Bi<sub>2</sub>NiMnO<sub>6</sub> with space group C2 (#5).

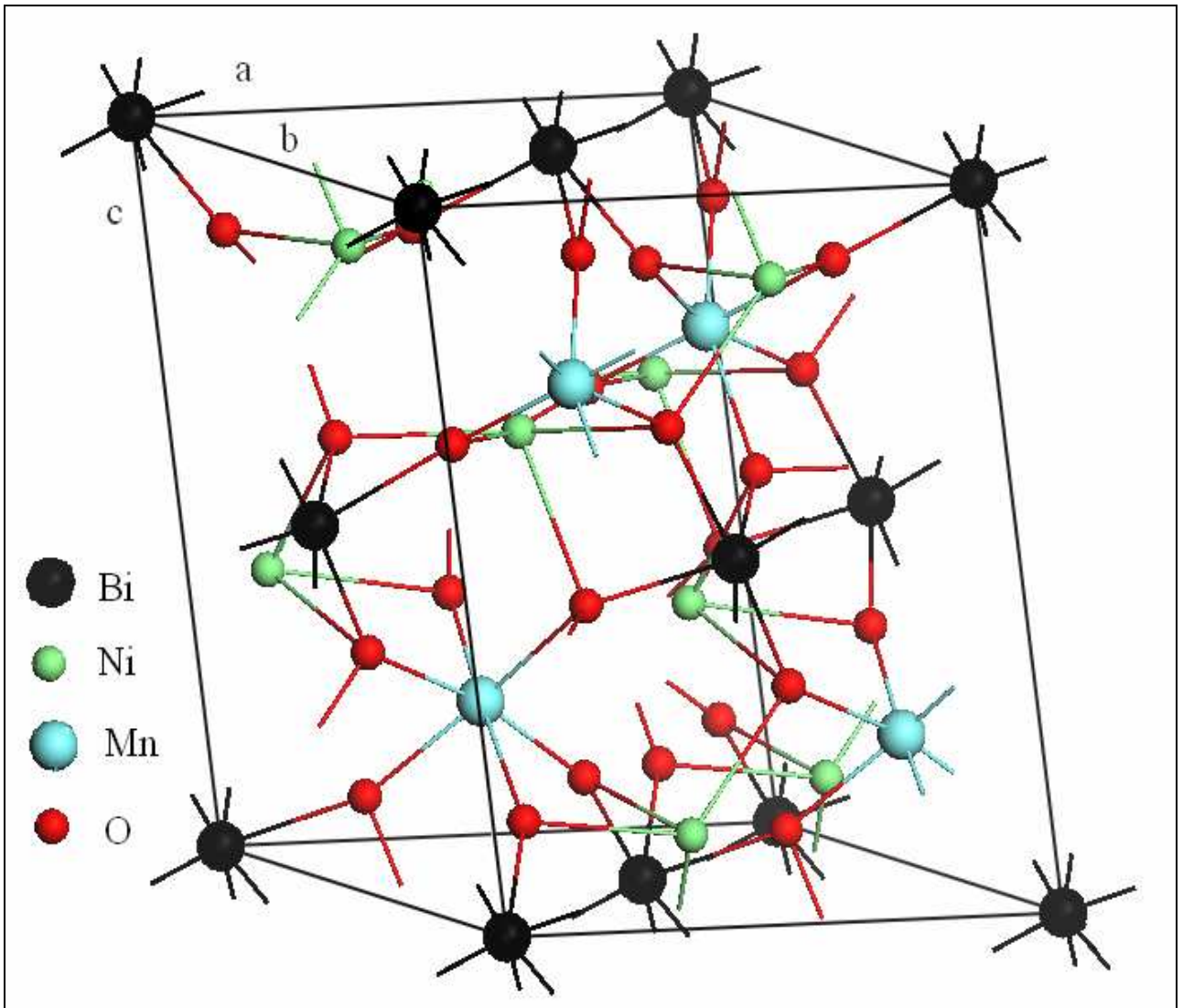


**Fig. 3.1.1:** Unit cell of  $\text{Bi}_2\text{NiMnO}_6$  containing four formula units.

The short axis is the **b** lattice vector which is perpendicular to the **a** and **c** vectors which make an angle  $\beta$  with each other. In *Table 3.1.1* the allowed positions of the atoms in the unit cell are tabulated according to the number of positions at each symmetry point and its Wyckoff label. The Greek letters signifying displacements along the lattice vectors are assumed to be relatively small and when they all vanish, the space group becomes the centrosymmetric  $C2/m$  (#12).

C2	C2/m	POSITIONS
2a	2a	(0, $\alpha$ , 0)
2b	2d	( $\frac{1}{2}$ , $\beta$ , $\frac{1}{2}$ )
4c	4i	(x, $\gamma$ , z) (-x, $\gamma$ , -z)
4c		(x, y- $\delta$ , z) (-x, y- $\delta$ , -z)
4c	8j	(x+ $\mu$ , -y, z+ $\eta$ ) [-(x+ $\mu$ ), -y, -(z+ $\eta$ )]

*Table 3.1.1: Space group symmetry of the crystal.*

The two-fold rotation about **b** is easily seen. For the 2a and 2b sites, the atoms go into themselves, mod a lattice translation. For the 4c sites pairs of atoms are interchanged by the rotation. Thus the electric polarization must lie along **b**. Note that the 4c's are of two different types, those emanating from 4i and those emanating from 8j. When  $\gamma = 0$  the 4ci sites go into themselves under a reflection in the **b** plane and into each other under inversion but when  $\mu$ ,  $\eta$ , and  $\delta = 0$ , under either reflection or inversion the 4cj sites within a single 4c do not transform amongst themselves, but rather into sites in the other 4c.

### 3.2 Results and Discussions.

In *Table 3.2.1* the calculated lattice constants and angle are compared with experiment. The agreement is excellent, with the GGA lattice constants being in better agreement with experiment than GGA+U but the GGA+U angle being in better agreement with experiment. The cohesive energy, amounting to about 6.6 eV per atom is

also given. A cohesive energy of this magnitude is indicative of strong covalent bonding. The effect of U on the total crystal energy is to reduce it by 6.27 eV; but because its effect on the atom is similar to its effect on the crystal, it only reduces the cohesive energy per 40 atom unit cell by 0.83 eV.

	a(Å)	b(Å)	c(Å)	$\beta(^{\circ})$	$E_c(\text{eV})$
<b>GGA</b>	9.501	5.418	9.634	107.884	264.50
<b>GGA+U</b>	9.557	5.447	9.680	107.848	263.67
<b>Expt<sup>61</sup></b>	9.465	5.423	9.543	107.823	

*Table 3.2.1: Lattice constants, angles and cohesive energies.*

atom	site	GGA			GGA+U			Experiment		
		x	y	z	x	y	z	x	y	z
<b>Ni</b>	<b>2a</b>	0.000	0.000	0.000	0.000	0.000	0.000	0.000	0.000	0.000
<b>Ni</b>	<b>2b</b>	0.500	0.030	0.500	0.500	0.032	0.500	0.500	0.015	0.500
<b>Mn</b>	<b>4c</b>	0.252	0.013	-0.251	0.252	0.013	-0.251	0.243	0.013	-0.251
<b>O</b>	<b>4c</b>	0.094	-0.042	-0.166	0.093	-0.043	-0.167	0.111	-0.061	-0.151
<b>O</b>	<b>4c</b>	0.414	0.056	-0.332	0.414	0.064	-0.331	0.420	0.042	-0.320
<b>Bi</b>	<b>4c</b>	0.135	0.016	0.375	0.137	0.017	0.378	0.133	-0.023	0.378
<b>Bi</b>	<b>4c</b>	0.373	0.042	0.125	0.372	0.042	0.124	0.364	0.035	0.123
<b>O</b>	<b>4c</b>	0.162	0.296	-0.370	0.162	0.299	-0.369	0.146	0.276	-0.364
<b>O</b>	<b>4c</b>	-0.154	-0.205	0.410	-0.156	-0.204	0.410	-0.157	-0.258	0.413
<b>O</b>	<b>4c</b>	0.356	0.220	-0.094	0.355	0.223	-0.092	0.377	0.204	-0.111
<b>O</b>	<b>4c</b>	-0.342	-0.282	0.140	-0.341	-0.280	0.139	-0.338	-0.284	0.126

*Table 3.2.2: Calculated atomic positions.*

In Table 3.2.2 the atomic positions within the unit cell are compared. The GGA and GGA+U agree well with each other but not as well with experiment. We think this may be a case where the theoretical results are more accurate than the experimental. It

seems unlikely that such accurate values for the lattice constants and angle could be obtained with sizable errors in the atomic positions. On the other hand, the experimental atomic positions were obtained by fitting the x-ray scattering factors with a superposition of ionic charge densities, including  $\text{Ni}^{2+}$  and  $\text{Mn}^{4+}$ . It is unlikely that fitting the charge density of a covalent crystal in this manner will lead to an accurate placement of the atoms. *Fig.3.2.1* is a plot of the GGA and GGA+U total DOS. (VASP is unable to obtain a spin-DOS from a spin-orbit calculation.) The GGA (GGA+U) energy gap is 0.448 eV (0.493 eV). The bonding Bi 6*p*, Mn and Ni 3*d*, and O 2*p* bands are over 6 eV wide and the sixteen Bi 6*s* bands are almost 2 eV below them.

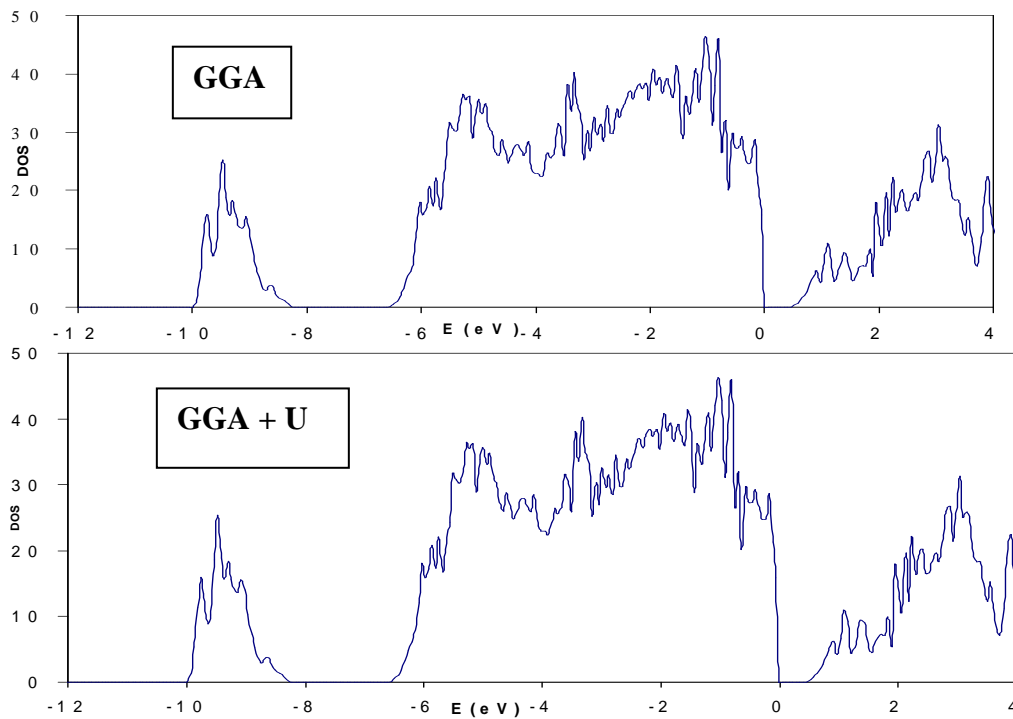


***Fig. 3.2.1: Density of states.***



The first three columns of the first five rows of *Table 3.2.3* are sums of the components of the magnetization in  $\mu_B$  per formula unit projected<sup>69</sup> on each kind of atom. The variation among atoms of a particular kind was negligible (except for the oxygen atoms, whose individual contributions are small) in the GGA+U and small in the GGA except the GGA calculation resulted in the Ni 2a and 2b sites having similar magnitudes but different directions of magnetic polarization. Here x and y are the **a** and **b** lattice vector components and z is the third Cartesian component (not along **c**).

	GGA							GGA+U						
	X	y	z	M	n	n <sup>↑</sup>	n <sup>↓</sup>	x	y	z	M	n	n <sup>↑</sup>	n <sup>↓</sup>
2a Ni	0.252	0.446	0.508	0.721	4.130	2.425	1.704	0.469	0.462	0.453	0.799	4.126	2.462	1.663
2b Ni	0.471	0.424	0.336	0.718	4.129	2.423	1.706	0.467	0.461	0.454	0.797	4.125	2.461	1.664
Mn	1.481	1.767	1.715	2.874	5.616	4.245	1.371	1.948	1.938	1.921	3.353	5.511	4.432	1.079
Bi	0.028	0.033	0.032	0.054	4.973	2.514	2.460	0.024	0.024	0.024	0.042	4.978	2.510	2.468
O	0.223	0.263	0.260	0.434	35.216	17.825	17.391	-0.066	-0.066	-0.064	-0.113	35.260	17.686	17.573
P <sub>T</sub>	2.454	2.933	2.850	4.800	54.064	29.432	24.632	2.841	2.820	2.788	4.878	53.999	29.552	24.447
Ξ <sub>T</sub>	2.539	3.042	2.954	4.942	63.000	33.971	29.029	2.907	2.885	2.853	4.991	63.000	33.996	29.005

**Table 3.2.3: Magnetic moments in  $\mu_B$  per formula unit.**

M is the magnitude of those projected components of magnetization, n is the number of electrons in each set of spheres, and the last two columns,  $n \pm M$ , are the projected number of majority and minority spins. The row labeled P<sub>T</sub> contains the sum of the above except for M which is the magnitude of the sums of the components, rather than the sum of the magnitudes. Note that although the projection spheres<sup>69</sup> encompass only 59% of the unit cell volume (in the GGA case), they contain 86% of its electronic charge and 97% of its magnetic moment. The Mn sphere contains 5.6 electrons implying an ionicity of no more than 1.4+ rather than the 4+ required if the oxygen were given its

nominal 2- ionicity. Ionicity is an ill defined quantity, depending on how the charge outside the spheres is assigned, and, more importantly, on the values chosen for the radii of the spheres. We note that our oxygen radius of 0.900 Å is much larger than the 0.66 Å given<sup>8</sup> for the radius of covalently bonded oxygen. The last row, labeled  $\Xi_T$ , contains the actual (unprojected) values of the previously mentioned items.

The GGA+U result,  $M = 4.99 \mu_B$ , is in near perfect agreement (and the GGA in very good agreement) with the predicted<sup>61</sup> value of  $5 \mu_B$  in the absence of antisite disorder. However, that prediction was based on the assumption that the manganese was  $Mn^{4+}$  with three majority and no minority spins which is very far from the case here. The GGA and GGA+U magnetizations point in slightly different directions which are far from the rotation axis and far from perpendicular to it. Note that because  $Bi_2NiMnO_6$  is a semiconductor, the deviation from an exact integer value for the magnetization (assuming  $g = 2$ ) is due to the spin orbit interaction and the small non-collinearity of the spins. The effect of the Hubbard U is to increase the majority and decrease the minority spin on the Ni and Mn while slightly decreasing their total charge. This is done at the expense of the oxygens which have a net projected majority spin in the GGA but net minority spin in the GGA+U.

The Berry phases<sup>58</sup> were calculated for an  $8 \times 8$  array of strings containing 16  $\mathbf{k}$ -points to obtain the electric polarizations  $\mathbf{P}'$  listed in *Table 3.2.4* for a set of fractional displacements between + and - 100% of the calculated displacements,  $\alpha$ ,  $\beta$ ,  $\gamma$ ,  $\delta$ ,  $\mu$ , and  $\eta$ . (The energy gap exists for all values of the displacements.) Because of the periodic boundary conditions imposed on the infinite crystal,  $\mathbf{P}$  is only defined mod a quantum of polarization  $\Delta\mathbf{P}$ , i. e.  $\mathbf{P} = \mathbf{P}' + n\Delta\mathbf{P}$  with  $\Delta\mathbf{P} = e\mathbf{b}/\Omega$  where  $e$  is the electronic charge,  $\Omega$  is

the unit cell volume, and  $\mathbf{b}$  is the lattice vector. We note that when the displacements vanish, so does  $\mathbf{P}'$  (there exist centrosymmetric cases<sup>60</sup> where  $\mathbf{P}' = \frac{1}{2}\Delta\mathbf{P}$ ) and that  $\mathbf{P}'$  varies approximately linearly with the displacements. The measured polarization is usually taken to be half of the difference between the positive and negative polarizations so  $\Delta\mathbf{P}$  can be ignored in cases where the centrosymmetric polarization vanishes and our calculated polarizations are  $16.839 \mu\text{C cm}^{-2}$  (GGA) and  $16.625 \mu\text{C cm}^{-2}$ .(GGA+U). These modest values are nevertheless large compared to the thin film experimental value of about  $5 \mu\text{C cm}^{-2}$ , perhaps because the thin film crystallized in a tetragonal perovskite structure due to the constraining effect of its perovskite substrate. The relatively small magnitudes of  $\mathbf{P}'$  and  $\Delta\mathbf{P}$  are a consequence of  $\mathbf{b}$  being much shorter than  $\mathbf{a}$  and  $\mathbf{c}$ .

	<b>GGA</b>	<b>GGA+U</b>
<b>100%</b>	16.839	16.625
<b>75%</b>	12.753	12.588
<b>50%</b>	8.443	8.342
<b>25%</b>	4.273	4.217
<b>0%</b>	0.000	0.000
<b>- 25%</b>	- 4.273	- 4.217
<b>- 50%</b>	- 8.443	- 8.342
<b>- 75%</b>	-12.753	- 12.588
<b>- 100%</b>	-16.839	- 16.625
<b><math>\Delta\mathbf{P}</math></b>	18.405	18.180

*Table 3.2.4: The GGA and GGA+U electric polarizations.*

The LDA and GGA “cubic” calculations of Ref. 24 resulted in exactly  $5 \mu_{\text{B}}$  on Mn and  $1 \mu_{\text{B}}$  on the Ni. Considering the hybridization, that these are exact integers is

surprising. They also obtained  $P = 28 \mu\text{C}/\text{cm}^2$  and mentioned that this was remarkably greater than the  $18 \mu\text{C}/\text{cm}^2$  obtained from the point charge model. Although our results are much closer to the point charge model, we agree with them that the point charge model can have large errors. We note that the calculated magnetizations of the crystal and its enantiomorph were found to be identical, as they must be because  $\mathbf{M}$  is a pseudovector and unchanged by inversion. In principle, if  $\mathbf{P}$  could be rotated through  $180^\circ$ ,  $\mathbf{M}$  might follow. Rotating the polarization by rotating an electric field seems possible for simple perovskites which are cubic except for a small distortion caused by the polarization, but, unfortunately, these are not magnetic. Rotating the polarization in a truly uniaxial crystal might be done by rotating the crystal in a strong electric field. However, the coupling between  $\mathbf{P}$  and  $\mathbf{M}$  in  $\text{Bi}_2\text{NiMnO}_6$  seems to be sufficiently weak that even if the  $\mathbf{P}$  could be rotated through  $180^\circ$ , it is unlikely that  $\mathbf{M}$  would follow. This conclusion was drawn from the fact that  $\mathbf{M}$  in the centrosymmetric crystal was found to be negligibly different from  $\mathbf{M}$  in *Table 3.2.3*. In the GGA+U case, for example,  $\mathbf{M} = (2.923, 2.8773, 2.8494) \mu_B$ .

## Chapter 4 DFT study of BaTiO<sub>3</sub>-LaMnO<sub>3</sub> heterostructure

Multiferroic materials form a class of compounds which have recently received a lot of attention from the material physics community. In order for a compound to belong to this group, it requires at least two order parameters to coexist in the same phase. Considering elastic, electric, and magnetic properties, there are three distinct groups of multiferroics: piezoelectrics, which have elastic and electric properties, piezomagnets, which have elastic and magnetic properties, and magnetoelectrics, where the ferro (or antiferro) electric and magnetic properties coexist. If the first two groups of multiferroics are relatively common, the magnetoelectric materials are much less so. A very important group of magnetoelectric multiferroics is formed by hexagonal rare-earth manganites which have the overall formula RMnO<sub>3</sub> (R = Y, Ho, Er, Tm, Yb, Lu, or Sc), and are ferroelectric but all are antiferromagnetic<sup>70-73</sup>.

Ferroelectric ferromagnets are extremely rare. One compound which has received a lot of attention recently is BiMnO<sub>3</sub>. It is well established that BiMnO<sub>3</sub> is a magnetic material with a magnetization of about 3.9  $\mu_B$  per formula unit, a fact supported by a number of experimental and theoretical papers<sup>53,74,75</sup> and it had also been believed to be ferroelectric with the noncentrosymmetric C<sub>2</sub> space group, a conclusion based on powder neutron diffraction experiments<sup>76,77</sup>. Seshadri and Hill<sup>3</sup> attributed this structure to the stereochemical activity of the Bi 6s<sup>2</sup> lone pair. However, very recently, Belik *et al.*<sup>57</sup> having used selected area electron diffraction, convergent beam electron diffraction, and Rietveld analysis of neutron diffraction data on polycrystalline samples, concluded that BiMnO<sub>3</sub> crystallizes in the centrosymmetric C<sub>2/c</sub> space group. Having first determined

that the actual structure depends sensitively on the oxygen stoichiometry<sup>78</sup>, Montanari, *et al*<sup>79</sup> used neutron studies on polycrystalline BiMnO<sub>3</sub> as a function of temperature and magnetic field to conclude the space group is C2/c. Battig, Seshadri and Spaldin<sup>80</sup> performed full computational structural optimizations of BiMnO<sub>3</sub> using the LDA+*U* method, finding the two proposed<sup>76,77</sup> polar C2 structures existed they are higher in energy than an antiferromagnetic centrosymmetric C2/c structure.

As far as we know, there are only two ferromagnetic ferroelectrics thus far synthesized (or three if one counts BiFeO<sub>3</sub>, an antiferromagnetic ferroelectric with a small spin canting, resulting in a negligible ferromagnetic moment, and which in a 70nm thick film was reported<sup>60</sup> to have a saturation magnetization of  $\sim 1 \mu_B$ ). One of these is Bi<sub>2</sub>NiMnO<sub>6</sub>. This compound was recently synthesized by Azuma *et al.*<sup>63</sup> as a heavily distorted double perovskite with four formula units in a monoclinic unit cell. We<sup>81</sup> recently reported the results of GGA and GGA+*U* calculations of Bi<sub>2</sub>NiMnO<sub>6</sub> in which the effects of spin-orbit and spin noncollinearity were included. A magnetization of 4.94  $\mu_B$ /f.u. (4.99 with *U*) and a polarization of 18.41  $\mu C/cm^2$  (18.18 with *U*) were obtained. The other compound of which we are aware was synthesized by Gajek *et al.*<sup>5</sup>. They reported that La<sub>0.1</sub>Bi<sub>0.9</sub>MnO<sub>3</sub> is a ferroelectromagnet which retains its properties down to a 2 nm thick film and have used it as a spin filtering tunnel barrier, the magnetization and electric polarization of which can be switched independently, giving rise to four different resistance states. The extraordinary challenge of creating these ferroelectromagnetic compounds suggests a superlattice approach. Murugavel *et al.*<sup>82</sup> have created a (PCMO)<sub>10</sub>(BST)<sub>9</sub> superlattice, where PCMO is ferromagnetic Pr<sub>0.85</sub>Ca<sub>0.15</sub>MnO<sub>3</sub> and BST is ferroelectric Ba<sub>0.6</sub>Sr<sub>0.4</sub>TiO<sub>3</sub>. The superlattice had Curie and Néel temperatures,  $T_C = 120$

K and  $T_N = 140$  K and showed a 40% magnetoresistance in a 7 T field at 80 K. Singh *et al.*<sup>83</sup> studied the structure of  $\text{La}_{0.7}\text{Ca}_{0.3}\text{MnO}_3/\text{BaTiO}_3$  superlattices of various size and measured magnetizations, ferroelectric polarizations, and Curie temperatures.

There are only two calculations of which we are aware that involve a ferroelectric interfacing with a ferromagnet. One involves a  $\text{Fe}/\text{BaTiO}_3$  superlattice. The authors<sup>84</sup> fixed the transverse lattice constant of the superlattice<sup>85</sup> at the experimental  $\text{BaTiO}_3$  lattice constant. Because this is smaller than their calculated  $\text{BaTiO}_3$  lattice constant, ferroelectric polarization in the longitudinal direction was assured. They found a  $0.37\mu_B$  difference between the sum of the Ti and Fe magnetic moments in the top and bottom interfaces (where “top” is the direction of  $\text{BaTiO}_3$  polarization) and suggested that if the magnetization of the surface of a few layers of iron on  $\text{BaTiO}_3$  could be controlled by changing the sign of the ferroelectric polarization, useful applications might be found. The centered  $2\times 2$  Fe lattice constant is larger than the  $\text{BaTiO}_3$  lattice constant to which it is nearly matched, so in actual fact, the transverse lattice constant of the superlattice will be slightly larger than that of  $\text{BaTiO}_3$  and the ferroelectric polarization will lie in the plane. The other calculation<sup>86</sup>, for a  $\text{Co}_2\text{MnSi}/\text{BaTiO}_3$  superlattice, calculated lattice constants, and found the Ti polarized at the  $\text{Co}_2/\text{TiO}_2$  interface but probably not at the  $\text{MnSi}/\text{TiO}_2$  interface.

In this paper we have present the results of completely relaxed electronic structure calculations for a  $\text{LaMnO}_3/\text{BaTiO}_3$  superlattice, similar to that described in Ref. 20 except for the replacement of  $\text{La}_{0.7}\text{Ca}_{0.3}\text{MnO}_3$  with  $\text{LaMnO}_3$ . The only reason for replacing  $\text{La}_{0.7}\text{Ca}_{0.3}\text{MnO}_3$  with  $\text{LaMnO}_3$  was to keep the calculation feasible even if, by doing so, we expected to replace the ferromagnetism of Ca doped  $\text{LaMnO}_3$  with the

antiferromagnetism of pure  $\text{LaMnO}_3$ . In the following Section we describe our computational method and in the last Section, we present and discuss our results.

#### 4.1 Computational Details

Our calculations were performed using the projected augmented wave<sup>34</sup> method as implemented in the VASP code<sup>35</sup>. The generalized gradient approximation<sup>24</sup> plus Hubbard  $U$  approximation<sup>87</sup> (GGA+ $U$ ) was used for the exchange-correlation energy density functional. In order to properly describe  $\text{LaMnO}_3$  as a semiconductor, we had to use the fairly large value of 7.5 eV for  $U - J$ , equal to the value obtained from  $2p$  core-level photoemission spectra<sup>88</sup> and less than the 9.22 eV obtained from “constrained” density functional calculations<sup>89</sup>. For Ti we assumed  $U - J = 0$ . The Brillouin zone was sampled with a  $7 \times 7 \times 3$   $\mathbf{k}$ -point grid. The basis set used contained all plane waves up to 20.79 Ry. The atomic positions were adjusted until all the forces on them were less than 10 meV/Å and the VASP code adjusted the lattice constants using a stress criterion based on the force criterion.

We originally constructed our superlattice to match that measured in Ref. 20, with four layers of  $\text{BaTiO}_3$  alternating with four<sup>90</sup> of  $\text{LaMnO}_3$ . However, we were unable to get the forces to converge. Because the forces at the  $\text{MnO}_2/\text{BaO}$  interface were much larger than those at the  $\text{LaO}/\text{TiO}_2$  interface, we constructed a superlattice with 4.5 layers of each compound which contained only  $\text{LaO}/\text{TiO}_2$  interfaces, and had no further convergence problems. This seems to confirm what was found in Ref. 21 and assumed to



be true in Ref. 23, namely, that the TiO<sub>2</sub> interface with a ferromagnet is much more stable than the BaO interface is with the ferromagnet.

## 4.2 Results and Discussion

The calculated lattice constants of<sup>91</sup> BaTiO<sub>3</sub> and<sup>92</sup> LaMnO<sub>3</sub> are compared with experiment in *Table 4.2.1*. Also listed are lattice constants for four formula units of BaTiO<sub>3</sub> for comparison with the LaMnO<sub>3</sub> unit cell. The discrepancies between theory and experiment are typical for density functional calculations, although the sign of the discrepancy in BaTiO<sub>3</sub> is unexpected with a GGA density functional. LaMnO<sub>3</sub> is triclinic but very close to being orthorhombic. This can be demonstrated by observing the ratio of the unit cell volume to the product of the lattice constants, 250.124/250.150 (calculated) and 243.569/243.592 (experiment).

	Lattice(Å)			
	a	b	c	vol
BaTiO <sub>3</sub>	3.9325	3.9325	3.9567	61.1886
	5.5614	5.5614	7.9134	244.7544
exp	3.992	3.992	4.036	64.317954
LaMnO <sub>3</sub>	5.5612	5.7607	7.8083	250.1240
exp	5.532	5.742	7.669	243.569
supercell	5.6498	5.7181	35.8470	1158.0591

*Table 4.2.1: Lattice constants.*

The LaMnO<sub>3</sub> magnetization was calculated to be 4.226 μ<sub>B</sub> per Mn in fairly poor agreement with the experimental value<sup>93</sup> of 3.7 ± 0.1 μ<sub>B</sub>. Better agreement could be

obtained with smaller values of  $U - J$ . For example,  $3.827 \mu_B$  was obtained with  $U - J = 3.5$  eV. Using the Berry phase method<sup>11</sup> the BaTiO<sub>3</sub> ferroelectric polarization was found to be  $27.05 \mu\text{C}/\text{cm}^2$ , in good agreement with the experimental value<sup>6</sup> of  $26.0 \mu\text{C}/\text{cm}^2$ .

The superlattice calculation was initiated with an antiferromagnetic Mn spin density similar to that of bulk LaMnO<sub>3</sub>, but it converged to a ferromagnetic distribution. One might suspect that an antiferromagnetic local energy minimum exists, but if it does, VASP manages to avoid it. The last row of *Table 4.2.1* lists the superlattice lattice constants. Note that the  $a$  and  $b$  constants are greater than the average of the BaTiO<sub>3</sub> and LaMnO<sub>3</sub>  $a$  and  $b$ . On the other hand,  $c$  and the unit cell volume are larger than 2.25 times the sum of BaTiO<sub>3</sub> and LaMnO<sub>3</sub>  $c$ 's and volumes, indicating a strong attraction between the LaO and TiO<sub>2</sub> planes forming the interface.

	Mn1	Mn2
outer	4.301	4.675
iner	4.256	4.26

*Table 4.2.2: Magnetization per manganese.*

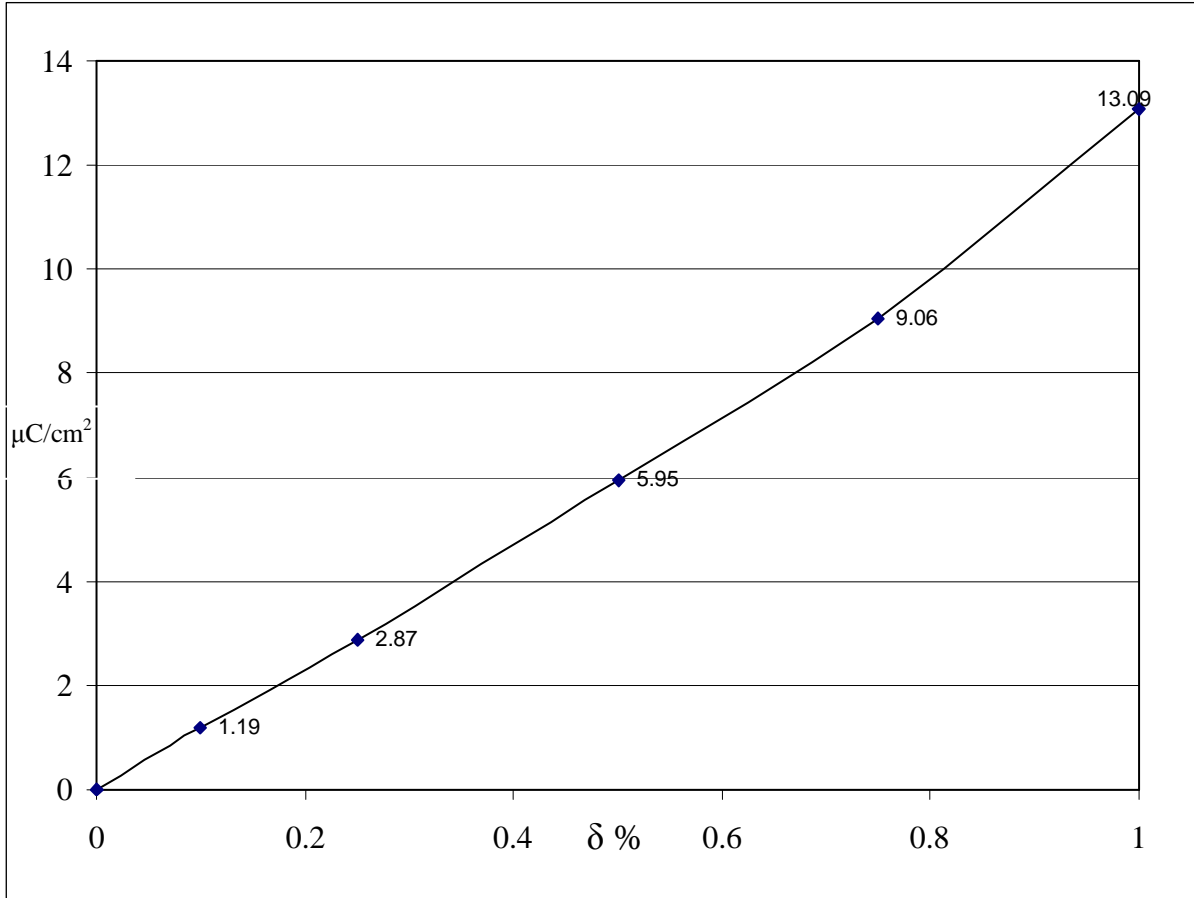
There are four Mn planes in the superlattice, each containing two inequivalent Mn atoms. The two inner planes are equivalent, as are the outer planes. The magnetization of these atoms is listed in *Table 4.2.2*. The two inner plane atom magnetizations are very slightly larger than those calculated for bulk BaMnO<sub>3</sub> whereas one of the outer two is slightly larger and one is much larger. This can be understood with an examination of the outer plane Mn bond lengths to their six neighboring oxygen atoms which are listed in

Table 4.2.3. Since covalent bonds are not magnetic and longer bond lengths imply less covalency, the Mn with the longest bonds are most magnetic.

bulk	Mn1	Mn2
1.938	2.006	2.146
1.938	2.009	2.147
2.041	2.028	2.153
2.041	2.021	2.155
2.078	2.115	2.078
2.078	2.186	2.155

**Table 4.2.3: Mn-O bond lengths.**

The calculated superlattice ferroelectric polarization is  $13.088 \mu\text{C}/\text{cm}^2$ . It lies along the direction in which the  $\text{BaTiO}_3$  is stretched by the  $\text{LaMnO}_3$ , i. e. along the  $b$  axis. It is about half as large as that calculated for bulk  $\text{BaTiO}_3$ , which was to be expected because the  $\text{BaTiO}_3$  constitutes about half of the volume of the superlattice. The polarization is uncertain to within some number of quanta<sup>11</sup>,  $\Delta\mathbf{P} = e\mathbf{b}/\Omega = 7.900 \mu\text{C}/\text{cm}^2$  where  $e$  is the electronic charge,  $\mathbf{b}$  is the lattice vector, and  $\Omega$  is the unit cell volume. To prove that no quanta should be added or subtracted from our result, we have calculated the polarization with the atoms displaced 75%, 50% 25% 10%, and 0% from their centrosymmetric positions and plotted the curve in *Fig. 4.2.1*. No other smooth curve can be drawn by subtracting any number of quanta from each point<sup>94</sup>.



***Fig. 4.2.1: Polarization as a function of displacement.***

It has been suggested<sup>95</sup> that in the case of a superlattice consisting of a ferroelectric and a metal where the Berry phase method is not applicable, one can estimate the polarization from the ratio of superlattice displacements away from centrosymmetry to those in the bulk crystal. It seemed that this would be a good opportunity to test that approximation. We have,  $P_{\text{est}} = (D/d)(v/V)P_{\text{bulk}}$  where  $D$  ( $d$ ) is the sum of the superlattice (bulk crystal) displacements for either Ti or O, and  $V$  ( $v$ ) is the superlattice (bulk crystal) unit cell volume.

	$P_{\text{cell}}$	$V$	$\delta\text{Ti}$	$P$	$\delta\text{O}$	$P$
<b>bulk</b>	27.05	61.18861	0.024799	-	0.029807	-
<b>supercell</b>	13.088	1158.059	0.020692	11.925	0.033566	16.094

*Table 4.2.4: Polarization results.*

In the first column of *Table 4.2.4*,  $P_{\text{bulk}}$  and  $P_{\text{supercell}}$  are listed. The remaining columns list the average (for ease of comparison) Ti and O displacements and  $P_{\text{Ti}}$  and  $P_{\text{O}}$ , the polarizations estimated therefrom. We see that  $P_{\text{Ti}} = 0.911 P_{\text{supercell}}$  and  $P_{\text{O}} = 1.230 P_{\text{supercell}}$ , and that their average,  $P_{\text{est}} = 1.070 P_{\text{supercell}}$ , is a reasonable approximation. The outer plane Mn are displaced relative to the inner plane Mn by  $0.33 \text{ \AA}$  and  $0.28 \text{ \AA}$  in the opposite direction to the Ti displacement along the  $\mathbf{b}$  lattice vector. This is not included in the approximate calculation and could account for its discrepancy with respect to the Berry phase calculation.

## Chapter 5 DFT study of $\text{Ge}_{1-x}\text{Mn}_x\text{Te}$

Diluted magnetic semiconductors (DMS) have been intensely studied because of their potential technological applications. The two important properties, which make DMS's so interesting, are their ferromagnetism and their semiconductor nature. A microdevice realized from a DMS, would have the tunability of a semiconductor (controlled by a gate voltage) and also memory storage capabilities due to its ferromagnetic nature. Even though this is a technological direction of great importance there remain obstacles such as weak ferromagnetic ordering and Curie temperatures, which are, in most of the cases, far below room temperature.

There are three main groups of DMS's: II-VI, III-V and IV-IV semiconductors doped usually with Mn, but also with several other transition metals (TM). The first two groups have received a lot of interest mainly for their promising increase in Curie Temperature  $T_c$ <sup>96,97</sup>, although the  $T_c$ 's reported to be above room temperature for<sup>98</sup> GaN and<sup>99</sup> ZnO have been questioned. Because the exchange mechanism causing ferromagnetism in all of these alloys is carrier induced ferromagnetism, it is particularly interesting to study the dependence of the magnetic properties as a function of the carrier concentration. For this purpose especially, it is very useful to study the IV-VI DMS,  $\text{Ge}_{1-x}\text{Mn}_x\text{Te}$ , where the Mn does not act as an acceptor (as it does in  $\text{Ga}_{1-x}\text{Mn}_x\text{As}$ ), which makes it possible to independently control both the carrier and TM concentrations.

This is a particularly convenient choice for experimentalists because of the high solid solubility limit of manganese ions in GeTe and a relatively high  $T_c$ .<sup>100</sup> Although the thermal equilibrium limit of Mn solubility in GeTe is  $x = 0.5$ , using the ionized cluster beam technique, Fukuma *et al.*<sup>101</sup> have achieved Mn concentrations in GeTe as high as  $x = 0.96$ . Also, Mn with five  $3d$  electrons, is the optimum candidate for enhancing the magnetism.

As far as we know there are no theoretical studies of the properties of  $\text{Ge}_{1-x}\text{Mn}_x\text{Te}$ . In this work, using an *ab initio* approach, we calculate different properties of this particular DMS as a function of both the Mn and hole concentrations. Questions to be answered are: Does the variation in magnetization that is found experimentally<sup>101-104</sup> as a function of the Mn and hole concentrations arise from a variation in the magnetic moments of the Mn ions or from a variation in the relative directions of those magnetic moments? And, does the large decrease of the magnetization which occurs at large Mn concentrations result from an antiferromagnetic interaction between nearest neighbor Mn's?

## 5.1 Computational Details

Our calculations were performed using the projected augmented wave<sup>34</sup> method as implemented in the VASP code<sup>35</sup>. The generalized gradient approximation<sup>24</sup> plus Hubbard U approximation<sup>87</sup> (GGA+U) was used for the exchange-correlation energy density functional. Assuming that the U for Mn in GeTe is the same as the U for Mn in GaAs, we took  $U - J = 3.5$  eV, since a value of U between 3 and 4 eV has been reported<sup>66</sup>

to be required to place the Mn *d*-bands correctly in GaAs. The spin-orbit interaction was included and the magnetization allowed to be non-collinear. The unit cell used in our calculation is a 4×4×4 GeTe supercell, containing 64 trigonal GeTe primitive unit cells. The Brillouin zone was sampled with a 5×5×5 **k**-point grid. The Mn 3*p* outer core electrons were treated as valence electrons. The basis set used contained all plane waves up to 19.84 Ry. Our convergence criterion for forces was 10 meV/Å (the VASP code automatically sets a stress criterion based on the force criterion), resulting in an energy convergence of 10<sup>-4</sup> eV per 128 atom unit cell (for any particular set of lattice constants and atomic positions, the energy was converged to 10<sup>-6</sup> eV). GeTe is always *p*-type and has been predicted<sup>105</sup> to have an equilibrium density of 5 × 10<sup>19</sup> Ge vacancies. Therefore we created holes by creating Ge vacancies (2 holes per vacancy). The Mn sites and vacancy sites were selected with the aid of a random number generator.

## 5.2 Results and Comparison with Experiment

In *Table 5.2.1* we have compiled data from Fukuma's group<sup>101-103</sup>. The chemical composition was measured by electron probe microanalysis, the magnetization with a SQUID magnetometer, and the carrier concentration was obtained from the ordinary Hall coefficient. The data from Ref. 8 are all taken with 20% Mn, presumably all of which are on Ge sites. In the first row where there are 27% Ge and 53% Te there must be 5.66% vacancies on the Ge sublattice. Similarly in the second row there must be 3.85% Ge sublattice vacancies and in the third and fourth rows there must be 1.96% Te sublattice vacancies. In addition there can be antisite defects and additional Te and Ge vacancies as



long as they occur in equal numbers. The carrier concentration, estimated from the Hall coefficient, appears<sup>106</sup> to increase with increasing Ge concentration, even though the number of vacancies required by the imbalance in the Ge and Te site occupations is decreasing. The magnetization increases with increasing hole concentration.

Ref	Composition	$P$	$M$
8	27:20:53	5.40E+19	0.49
8	28:20:52	1.72E+20	0.78
8	31:20:49	2.29E+21	1.08
8	31:20:49	2.56E+21	1.14
7	$x=0.13$	2.12E+21	2.38
6	$x=0.12$	7.09E+20	0.865
6	$x=0.24$	1.12E+21	1.130
6	$x=0.51$	6.51E+20	0.600
6	$x=0.69$	2.93E+20	0.03
6	$x=0.78$	6.1E+19	0.01

*Table 5.2.1: Compilation of the experimental magnetization in  $\mu_B$  per Mn for various compositions and number of carriers per  $cm^3$ .*

The concentrations of the remaining samples in *Table 5.2.1* are given in terms of  $x$ . If this is the  $x$  in  $Ge_{1-x}Mn_xTe$ , the number of Te vacancies must equal the number of Ge vacancies, which is not likely to be the case. We therefore will assume  $x$  represents the percentage of Ge lattice sites, including those with vacancies that are occupied by Mn. In Ref. 7 several Ge(TM)Te samples were compared. The only Mn sample there is of interest because its magnetization,  $2.38 \mu_B$  per Mn, is more than twice that of any of the nine samples in Refs. 6 and 8. In Ref. 6 the magnetization is determined as a function of  $x$ . It maximizes at, or perhaps slightly beyond,  $x = 0.24$ , then falls slowly to  $x = 0.51$  and then drops precipitously to a negligible value at  $x = 0.69$ . Unfortunately, the number of holes, which is not controllable, happens to track the magnetization perfectly, so it is not

possible to draw any firm conclusions concerning the composition dependence of the magnetization.

We<sup>107</sup> have previously calculated the pressure at which trigonal GeTe undergoes a phase transition to the rock salt structure. A similar transition is reported<sup>101</sup> at  $x = 0.18$  in bulk  $\text{Ge}_{1-x}\text{Mn}_x\text{Te}$  and at  $x = 0.2$  in thin films. Because there are only a small number of random Mn atoms and vacancies per supercell, our relaxed crystal lattice is triclinic, but approximates a trigonal or cubic crystal as seen in *Table 5.2.2*, where we list the average cubic angle and lattice constant.

$x$	$v$	$\alpha$	$a$ (Å)
0.156	0	89.9543°	23.296
0.156	1	89.9807°	23.295
0.156	2	89.9886°	23.295
0.156	3	89.9896°	23.295
0.313	3	89.9910°	23.079
0.469	3	89.9921°	22.926
0.625	3	89.9928°	22.787

*Table 5.2.2: Average lattice angles and lattice constants.*

The three angles differ by  $0.0066^\circ$  ( $0.0014^\circ$ ) for  $x = 0.156$  and zero (one) vacancy. For all other cases the variation is  $0.0007^\circ$  or less. It is interesting to compare the zero vacancy case with our GeTe GGA calculation. There  $\alpha = 88.06^\circ$  and the polarization, using the modern theory of polarization<sup>11</sup>, was calculated to be  $64.9 \mu\text{C}/\text{cm}^2$ . Considering that  $(90^\circ - \alpha)$  for  $x = 0.156$  is only 2.4% as large as that for  $x = 0$ , our calculated value of  $35.0 \mu\text{C}/\text{cm}^2$  for the  $x = 0.156$  polarization is surprisingly large. Because filled bands are required to calculate Berry phases<sup>11</sup>, we could not check whether any of the vacancy containing cases were polarized. It seems reasonable that any case

with  $\alpha \geq 89.99^\circ$  would be exactly cubic if the supercell were large enough to insure complete randomness. Thus our calculation suggests that for a large enough number of hole carriers, the phase transition occurs for  $x \leq 0.156$ .

Mn	$x$	$p$	M	Mproj	Nproj
10	0.156	0.00	0.12	4.23 - 4.27	4.92 - 4.93
10	0.156	6.33E+20	2.39	4.21 - 4.26	4.92 - 4.93
10	0.156	1.27E+21	2.81	4.19 - 4.25	4.92 - 4.93
10	0.156	1.90E+21	3.12	4.16 - 4.23	4.92 - 4.94
20	0.313	1.91E+21	3.88	4.18 - 4.27	4.91 - 4.94
30	0.469	1.92E+21	2.47	4.17 - 4.25	4.92 - 4.94
40	0.625	1.93E+21	0.89	4.15 - 4.24	4.92 - 4.94

**Table 5.2.3: Total and projected magnetizations in  $\mu_B$  per Mn.**

The first column of *Table 5.2.3* lists the number of Mn atoms in each of our calculations and the second column lists the fraction of the 64 Ge lattice sites they occupy. The hole densities listed in column four result from zero to three Ge vacancies, each of which results in two holes. The very slight increase in  $p$  with increasing Mn concentration results from a decrease in the supercell volume with Mn substitution. The fourth column lists the total magnetization in  $\mu_B$  per Mn atom. We see from the first four entries that for a fixed number of Mn, the magnetization increases monotonically with the hole density, as observed experimentally, and from the last four entries that for essentially constant hole density, the magnetization peaks at intermediate values of  $x$ , which was indicated by experiment but could not be verified because the hole density could not be controlled. We projected the x, y, and z components of the Mn  $d$ -electron magnetization on every Mn to obtain the range of Mn magnetizations shown in the fifth column. Since the individual Mn all have a magnetization of  $4.21 \pm 0.06 \mu_B$ , the first

question asked in the Introduction is answered. The variation in the magnetization with Mn density and hole density, is caused by a variation in the relative Mn spin orientations and not by a variation in their magnitudes. To answer the second question, we performed a calculation with two nearest neighbor Mn and one vacancy. To the accuracy of the calculation, 0.1 meV, the energy was independent of the relative orientation of the spins. Thus we conclude that the precipitous drop in magnetization that occurs when the Mn density gets large, is not due to an antiferromagnetic interaction between nearest neighbor Mn but may be due to the formation of MnTe clusters, since MnTe is antiferromagnetic (although in a different crystal structure). The last column of *Table 5.2.3* lists the maximum and minimum number of projected Mn  $d$  electrons in each case. From  $M_{\text{proj}}$  and  $N_{\text{proj}}$  the number of majority and minority spin  $d$ -electrons on each Mn can be determined. This averages to 4.57 majority and 0.36 minority spins. A final comment on these results is that the  $M = 0.12 \mu_B$  obtained with no carriers is undoubtedly an artifact of the small number ( $N = 10$ ) of randomly oriented spins. We expect  $M$  would vanish in this case as  $N^{-1/2}$ .

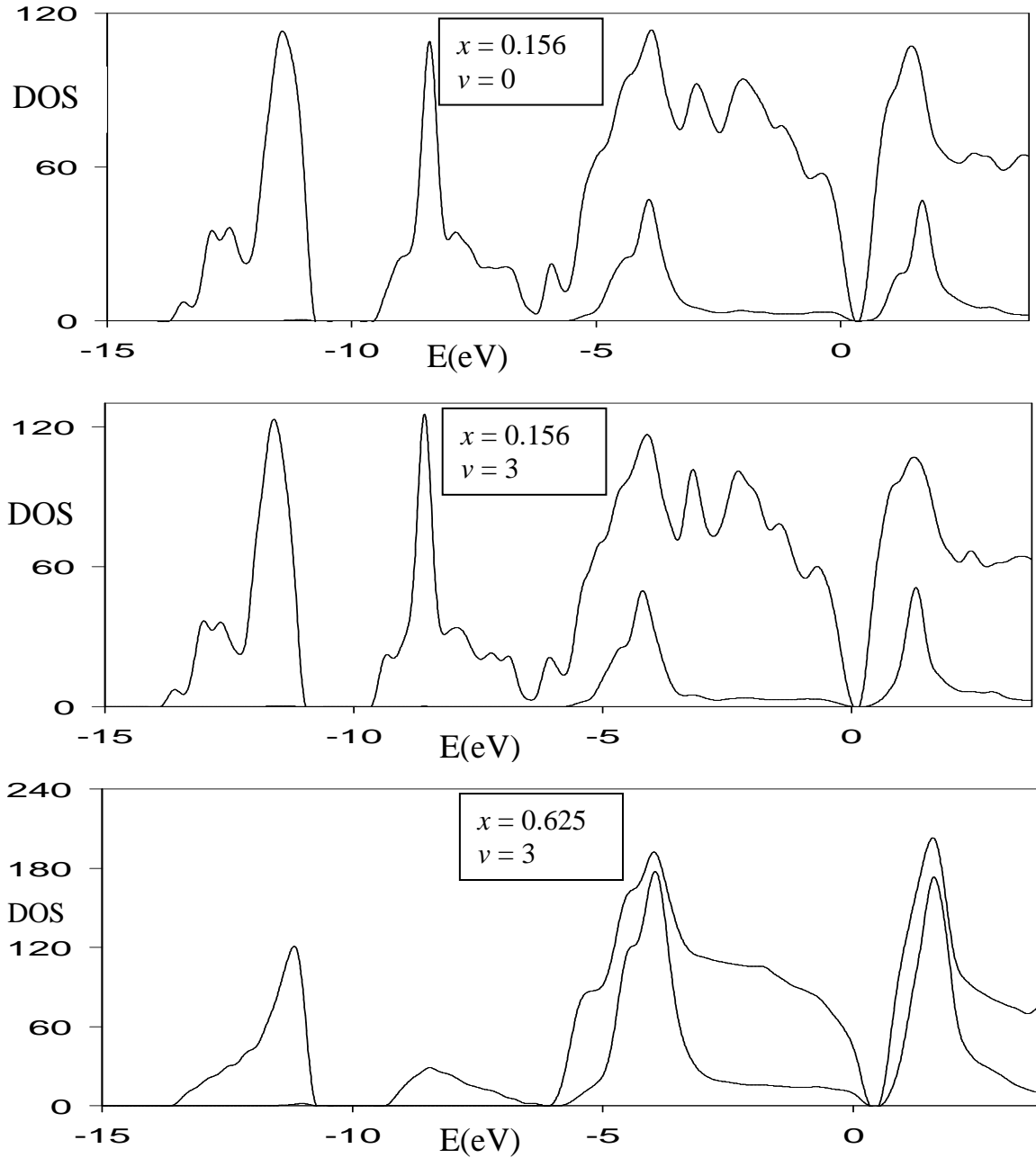


**Fig. 5.2.1: Total and projected Mn  $d$  densities of states.**

Figure 5.2.1 displays the total density of states (DOS) as well as the Mn  $d$  DOS for  $x = 0.156$ ,  $\nu = 0$ ; for  $x = 0.156$ ,  $\nu = 3$ ; and for  $x = 0.625$ ,  $\nu = 3$ . The zero of energy is, in each case, the highest occupied level and the hole Fermi energy then becomes the

energy at the top of the valence bands. The split off DOS at the lowest energy is comprised of Te  $s$  bands, the nearly split off DOS above it are Ge  $s$  bands and everything else consists of GeTe  $p$  bands and Mn  $d$  states. We cannot refer to the nearly 6 eV exchange split Mn  $d$  DOS as being between up and down spin bands since “up” points in a different direction on each Mn ion. We note that increasing number of Ge vacancies from zero to three, removes 12 Ge states, adds 6 vacancy states within the valence bands and leaves 6 holes at the top of the valence bands but otherwise has only a very minor effect on the DOS. On the other hand, going from  $x = 10$  to  $x = 40$  smears out much of the structure as well as increasing the Mn contribution by a factor of four and decreasing the Ge by a factor of 7/17.

For the same values of  $x$  and  $v$ , in *Fig. 5.2.2* we plot the energy bands around the energy gap from  $\Gamma$  to what would be the X and L points in the Brillouin zone (BZ), if the supercell was perfectly cubic. Examining the entire BZ we find that the top of the valence bands is at L and the bottom of the conduction bands is at  $\Gamma$ . We note that the bands with  $x = 0.625$  are much flatter than the others and that this results in a wider energy gap. In Ref. 8 Fukuma *et al.* plotted the energy gap (from the highest occupied valence band state to the bottom of the conduction bands) for constant  $x$  as a function of  $p^{2/3}$ . Because, as is often the case with density functional calculations, our energy gap is about half of the experimental gap.

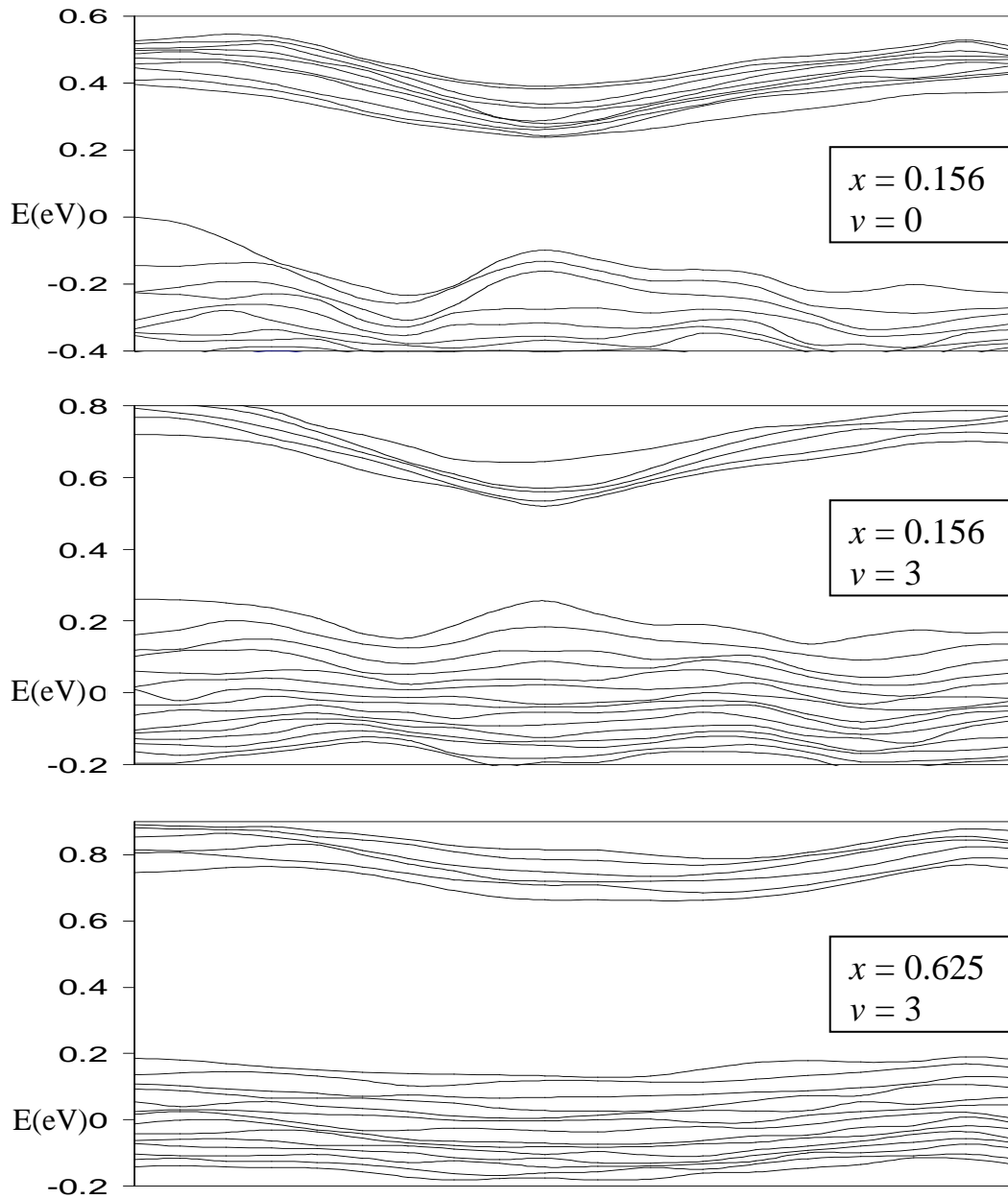


*Fig. 5.2.2 Energy bands around the energy gap for the values of  $x$  and  $\nu$  shown.*

In *Fig. 5.2.3* we compare their energy from the highest occupied state to the top of the valence bands (i. e. the hole Fermi energy) with ours. There are several reasons not to expect our results to agree. Their  $x = 0.20$ , our  $x = 0.156$ . Our carriers are due only to Ge

vacancies; theirs are due to both Te and Ge vacancies and, undoubtedly, a few other imperfections. That their magnetization is less than ours could be blamed on our calculations, but the fact that it is less than half they obtained 15 months later<sup>102</sup> in a crystal with 1/3<sup>rd</sup> fewer carriers and only 65% of the Mn indicates that the quality of this set of samples is not as great as they were able to achieve later.

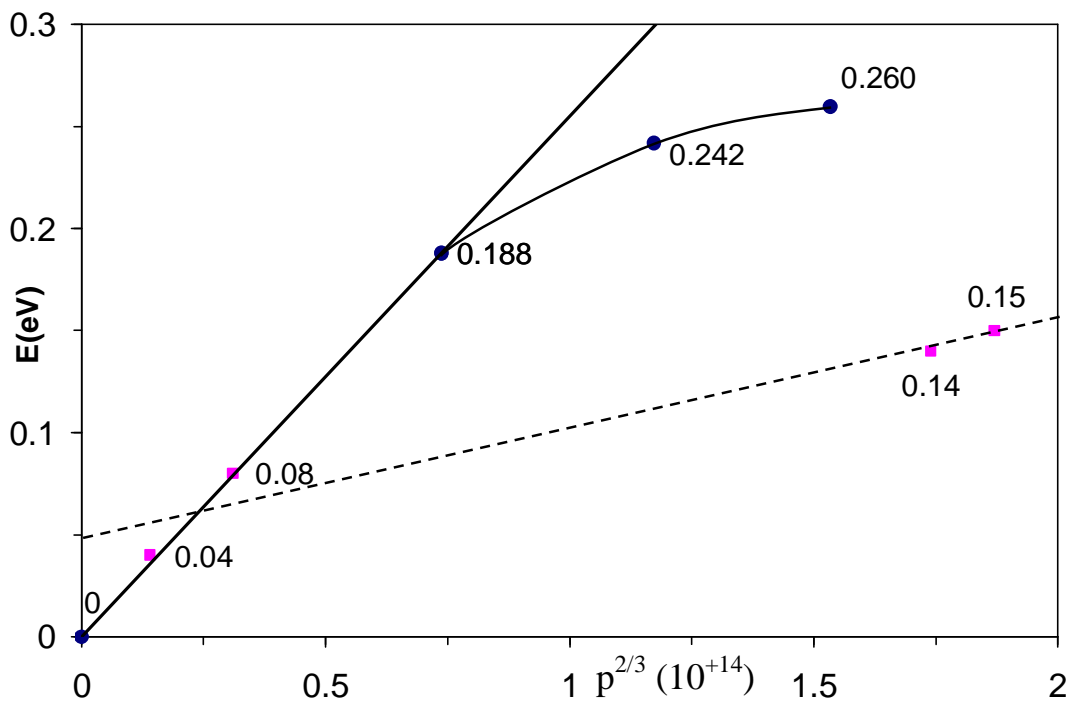


**Fig. 5.2.3: Hole Fermi energies vs. hole density per  $cm^3$**

Therefore it is surprising that their first two points lie on the straight line between our first two points. That the curve flattens out for larger values of  $p^{2/3}$  where more bands contribute and the energy of the original bands no longer increases as  $k^2$  is easily understood. The dashed line was drawn by Fukuma *et al.* and represents what they



perceive to be the best fit to their data. It cannot be taken too seriously, however, because it says that when there are no holes, the holes have a Fermi energy of 0.5 eV.

In summary, we have shown that each Ge vacancy in  $\text{Ge}_{1-x}\text{Mn}_x\text{Te}$  creates two holes and that the magnetization increases monotonically with the number of holes. The total magnetization increases up to about  $x = 0.5$  and drops precipitously beyond that. The magnetic moment of the Mn ions was always within  $0.06\mu_B$  of  $4.21\mu_B$  and the variation in the total magnetization results from the degree of their noncollinearity.

## Chapter 6 DFT study of Si(001)/Si(110) and Si(100)/Si(110) interfaces

Electrons and holes both have their highest mobility in the  $\langle 110 \rangle$  direction in silicon but this occurs at a (001) face for electrons and a  $(-110)$  face for holes. Thus Hybrid Orientation Technology (HOT) is currently a subject of intense activity in the device community<sup>108, 109</sup>. One way to have p and n type circuits in close proximity in a bulk like Si environment is to directly bond two (or more) silicon substrates of different orientations to each other<sup>110</sup>. Although it was not their intended use, we<sup>111</sup> have recently measured the I-V curves *through* directly bonded Si(001) and Si(110) slabs. In our case the two slabs were as identical as possible, each doped with  $10^{15}$  boron atoms per  $\text{cm}^3$ . The current obtained was extremely asymmetric as seen<sup>112</sup> in Fig. 6.1 where the current at  $-2$  V is more than four orders of magnitude larger than the current at  $+2$  V.

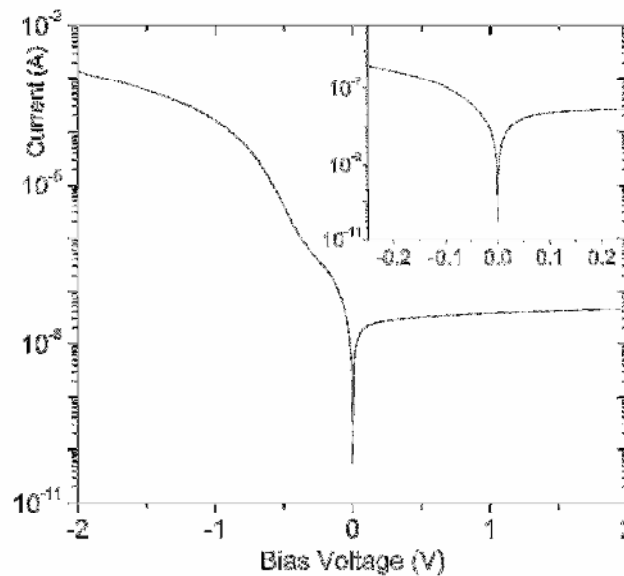


**Fig. 6.1:** Current vs. voltage curve for a Si(110)/Si(001) junction.

Valence band offsets were used in a conventional device simulator (which ignores all quantum mechanical aspects of the interface) to generate I-V curves. These did not fit the experimental data very well but did result in a four order of magnitude asymmetry when a step function potential of 0.4 eV, representing the valence band offset, was used.

### 6.1 Calculations and results

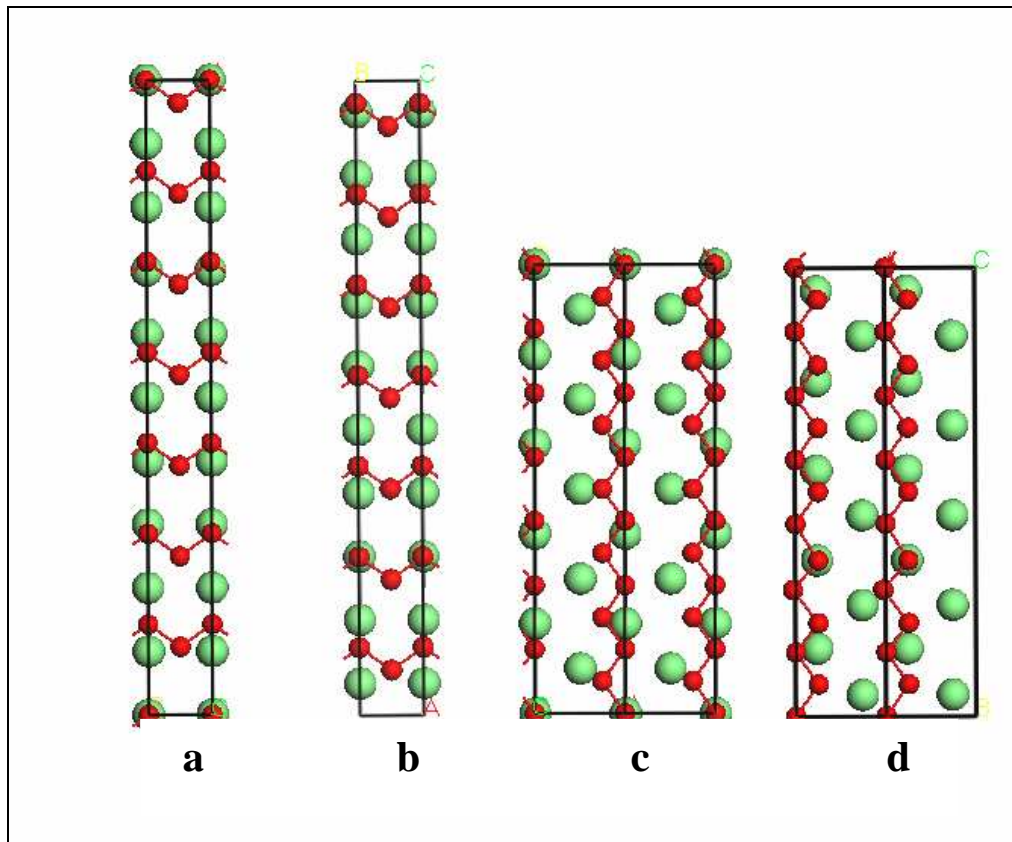


**Fig. 6.1.1: The Si(110)/Si(001) unrelaxed interfaces for 2 different orientations.**

We here report on those properties of Si(001)/Si(110) and Si(100)/Si(110) interfaces that can be obtained from density functional superlattice calculations. In Fig. 6.1.1 fits of

the unrelaxed (001) and (100) surface planes with the (110) surface plane are displayed for both the interfaces in the supercells we will use. The (110) surface planes' unit vectors are (001) and  $(-\frac{1}{2}\frac{1}{2}0)$ . The (001) surface planes' unit vectors can be chosen to be  $(-\frac{1}{2}\frac{1}{2}0)$  and  $(\frac{1}{2}\frac{1}{2}0)$  as in *Fig. 6.1.1 (a,b)* (hereafter called orientation A) and the (100) surface plane's can be chosen to be (010) and (001) as in *Fig. 6.1.1 (c,d)* (orientation B). In *6.1.1 (a,b)* the  $(-\frac{1}{2}\frac{1}{2}0)$  vectors are common to both faces and 10  $(\frac{1}{2}\frac{1}{2}0)$  unit vectors match 7 (001), to within 1.0%. In *6.1.1 (c,d)* the (001) vectors are common to both faces and 5 (010) match 7  $(-\frac{1}{2}\frac{1}{2}0)$  unit vectors, also to within 1.0%. Note that the two interfaces in either configuration differ only by a translation. *Figs. 6.1.1 (c)* and *6.1.1 (d)* differ by both a longitudinal and a transverse translation which is the reason for showing two unit cells. Thus, although there is no symmetry associated with either superlattice, planar averages of the charge density or potential should have reflection symmetry, Examining *Fig. 6.1.1*, we see that in both cases there are 10 atoms in the (001) or (100) planar unit cell and 14 in the (110) planar unit cell. With 14 (001) or 14 (100) planes and 10 (110) planes there are 140 Si atoms in each quantum well and both wells have the same length to within 1.0 %.

The calculations were performed using the projected augmented wave method<sup>34</sup> as implemented in the VASP software package<sup>35</sup>. The PBE<sup>24</sup> form of the generalized gradient approximation (GGA) was used for exchange and correlation. Seven k-points were sampled in the Brillouin zone (BZ) and all  $K^2 < 11$  Ry were included in the plane wave basis set. By reducing the forces on the atoms so that none was larger than 0.014 eV/Å and minimizing the stresses<sup>113</sup>, the atomic positions and supercell dimensions were optimized, resulting in the atomic positions and cell dimensions displayed in *Figs. 6.1.2*

and 6.1.3 for the two orientations. Note that the stress relaxation allows the 1% strain, introduced when constructing the planar cell, to be shared in the optimum way between the two quantum wells and to have a negligible effect on the results.

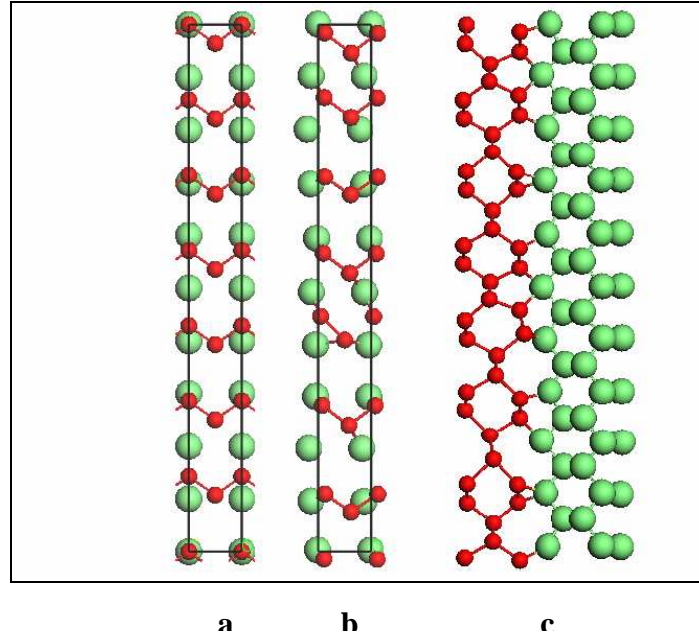


**Fig. 6.1.2:** (a) Unrelaxed and (b) relaxed  $\text{Si}(110)/\text{Si}(001)$  interface planes and (c) a side view of the relaxed interface.

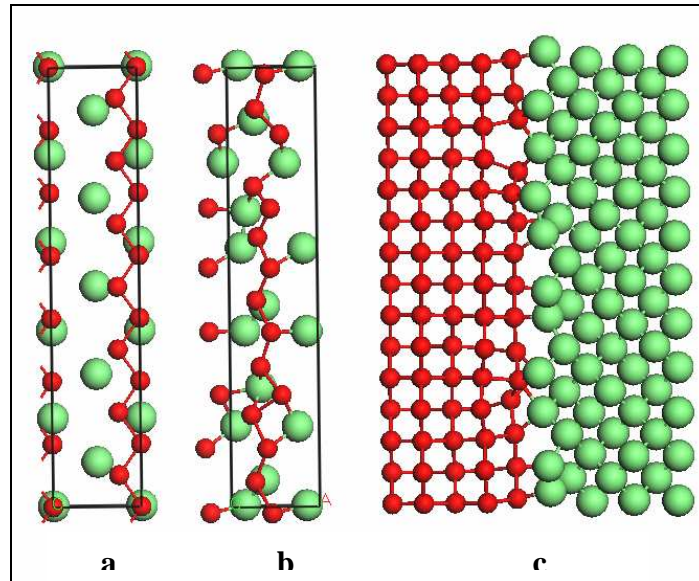


**Fig. 6.1.3: Same as Fig. 6.1.2 except for Si(110)/Si(100).**

In Figs. 6.1.2 (a) and 6.1.3 (a) we again display the two interfacial unrelaxed unit cells for comparison with the relaxed planar unit cells in 6.1.2 (b) and 6.1.3 (b). Figs 6.1.2 (c) and 6.1.3 (c) display side views of the interfaces. Normal to the page in 6.1.2 (c) [4(c)] is the  $(-\frac{1}{2}\frac{1}{2}0)$  [(001)] unit vector common to both interfacial unit cells. Note that a (110) surface has one dangling bond per atom while (001) and (001) surfaces have two per atom. Thus the ten (001) or (100) atoms present 20 dangling bonds to the 14 dangling bonds from the fourteen (110) atoms. It is clear from Fig.6.1.2 (c) that every (110) dangling bond forms a covalent bond with one of the (001) dangling bonds, leaving six (001) bonds dangling. In Fig. 6.1.3 (c) we see a much more distorted interface. There is a broken bond in the (110) interfacial plane, resulting in a pentagonal loop and increasing the number of (110) dangling bonds to 16, each of which form a covalent bond with a (100) dangling bond. There are also two dimmers in the (100) interfacial plane, similar to those in the Si(100)  $2\times 1$  surface reconstruction. Thus there are no (100) dangling bonds. Our calculated bulk Si lattice constant is  $a = 5.445 \text{ \AA}$ , making the bulk (001) and (100) interplanar spacing,  $a/4 = 1.361 \text{ \AA}$  and the bulk (110) interplanar spacing,  $a\sqrt{2}/4 = 1.925 \text{ \AA}$ . The spacing between the average positions of the rumped interfacial planes in orientation A (B) is  $1.832 \text{ \AA}$  ( $1.859 \text{ \AA}$ ), which are markedly larger than the  $1.643 \text{ \AA}$  average of the two bulk interplanar spacings and just a little less than the (110) spacing.

We define the interface energy to be the energy cost to create an interface, i. e.

$$(1) \quad E(\text{interface}) = [E(\text{supercell}) - 280 E(\text{Si})]/2A,$$

where our calculated values of the bulk Si total valence electron energy and the two supercell total energies and areas, A [in *Figs. 6.1.2 (b)* and *6.1.3 (b)*], are listed in *Table 6.1.1* along with the interfacial energies obtained from them, 86 and 67 meV/Å<sup>2</sup>, for configurations A and B respectively.

	<b>Si(110)/Si(001)</b>	<b>Si(110)/Si(100)</b>
<b>E(Total)</b>	-30346.8817 eV	-30352.5855 eV
<b>E(Si)</b>	-108.47239 eV	-108.47239 eV
<b>Area</b>	147.40 Å <sup>2</sup>	146.72 Å <sup>2</sup>
<b>E(Interface)</b>	86 meV/ Å <sup>2</sup>	67 meV/ Å <sup>2</sup>
<b>E(Adhesion)</b>	100 meV/ Å <sup>2</sup>	119 meV/ Å <sup>2</sup>
<b>V B Offset</b>	86 meV	93 meV
<b>Interface Bands</b>	10	0
<b>IPS</b>	1.832 Å	1.859 Å

*Table 6.1.1: Important quantities which describe the interface.*

Because configuration B resulted in no dangling bonds, it is not surprising that it costs configuration A (with its six dangling bonds) more energy to have its interfaces. The energy to separate the two slabs, i. e. the adhesion energy, is the energy to create their surfaces minus the interface energy,

$$E(\text{adhesion}) = E(\text{110 surface}) + E(\text{001 surface}) - E(\text{interface}). \quad (2)$$

We estimate this using the experimental values<sup>114</sup>,  $E(\text{110 surface}) = 118.6 \text{ meV}/\text{Å}^2$  and  $E(\text{001 surface}) = 76.8 \text{ meV}/\text{Å}^2$  to obtain  $100 \text{ meV}/\text{Å}^2$  for the configuration A adhesion energy and  $119 \text{ meV}/\text{Å}^2$  for configuration B (also listed in *Table 6.1.1*). In *Fig. 6.1.4* we

display the planar averages of the coulomb plus exchange-correlation potentials. Although there are no symmetry operations in the superlattice of either configuration, any failure of the planar average of the potential to have reflection symmetry is a result of incomplete convergence of the relaxed atomic positions.

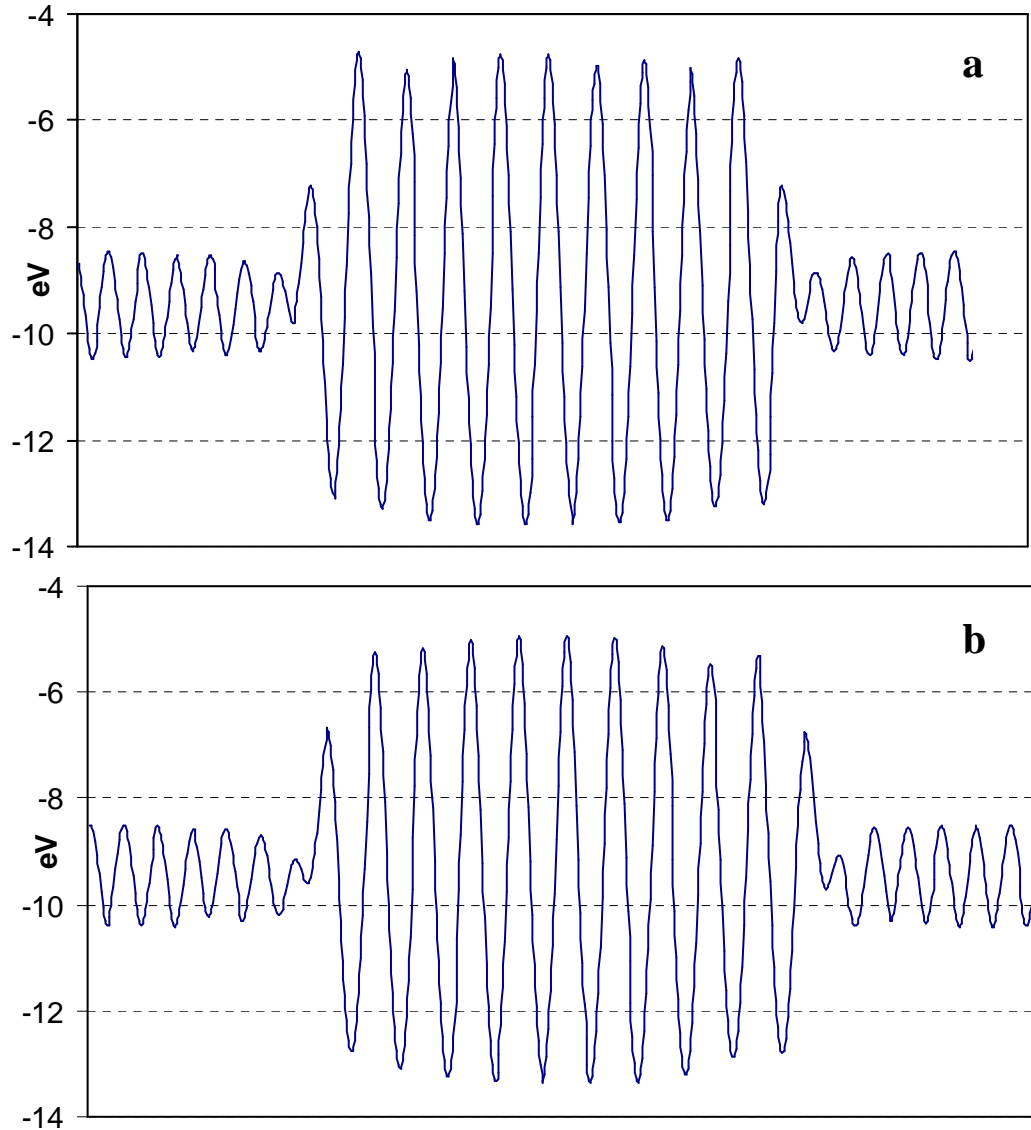


**Fig. 6.1.4: Planar average of the coulomb plus exchange-correlation potential for (a) Si(110)/Si(001) and (b) Si(110)/Si(100) supercells.**



The valence band offsets are obtained by averaging the potentials over a single bulk unit cell in the interior of each quantum well and taking the difference. The Si(110) interior average potential was found to be 86 meV [93 meV] more negative (i.e. attractive for electrons, repulsive for holes) than the Si(001) [Si(100)]. These valence band offsets are also listed in *Table 6.1.1* It is interesting to note that although the Si(100)/Si(110) interfaces have a greater valence band offset and a larger adhesion energy, only the Si(001)/Si(110) interfaces are being made. Because the manufacturing technique is proprietary, we do not know whether this is due to a difficulty in the manufacture of configuration B junctions or poor electronic properties resulting from the roughness of their interfaces, making them of no practical use.

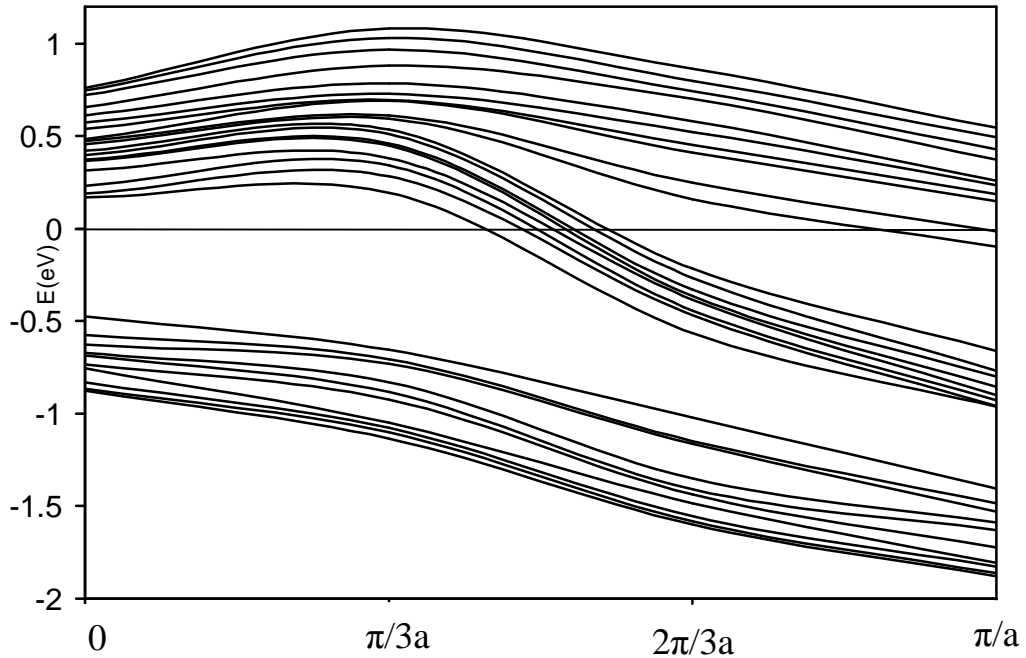


*Fig. 6.1.5: Energy bands around the Fermi energy of Si(110)/Si(001).*

The Si(110)/Si(001) energy bands near the energy gap are displayed in *Fig. 6.1.5* in the only direction in which the BZ is large enough to allow any dispersion. Because there are 280 atoms in the supercell, the 560<sup>th</sup> band might be expected to be at the top of the valance bands, but, in fact, band 256 is at the top of the valence bands. The number of interface bands (20, including a factor of 2 for spin) does not seem to be directly related to the number of dangling bonds (12, including a factor of 2 for two interfaces). The Fermi energy will be pinned where it is in *Fig. 6.1.5*, making unrealistic the simple model of a step function valence band offset screened by boron supplied holes, which we used in Ref. 111. It is unclear whether the experimental I-V curves could be reproduced by a classical model, where electrons would flow out of a thin central region to screen a step of height  $E_F - E(\text{vb})$  on one side and  $E_F - [E(\text{offset}) + E(\text{vb})]$  on the other. Here  $E(\text{vb})$  is the energy at the top of the valence bands.

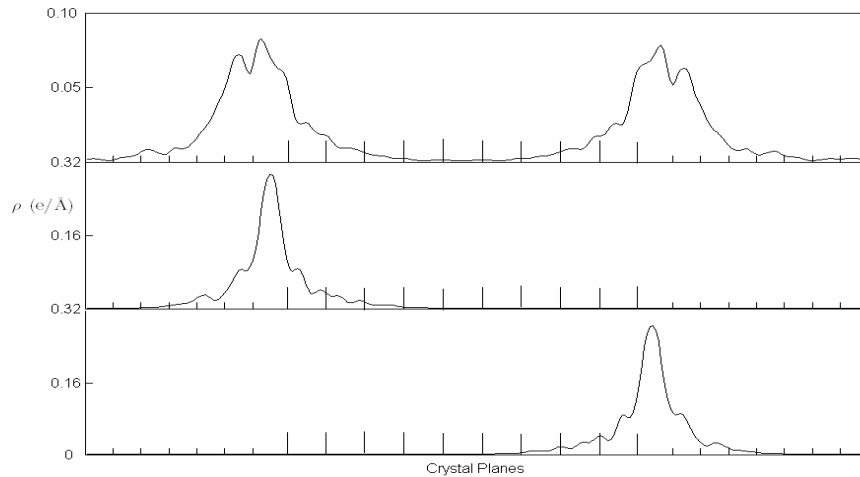


**Fig .6.1.6: Interface states at  $k = \pi/2a$  for the (a) 268th band, (b) 258<sup>th</sup> band, and (c) 259<sup>th</sup> bands of Si(110)/Si(001).**

The planar average of three of the interface state wave functions' absolute values squared is plotted in *Fig. 6.1.6*. These are from the 559<sup>th</sup>, 560<sup>th</sup>, and 568<sup>th</sup> bands at  $k =$

$\pi/2a$ . If the interfaces were so far apart that there was no overlap between interface states on different interfaces, and if the atomic relaxation were completely converged, there would be degenerate states on the two interfaces whose planar averaged charge density was identical, as is approximated by Figs. 6.1.6 (b) and (c) and these degenerate states could be combined to obtain states whose planar averaged charge density had reflection symmetry as Fig 6.1.6 (a) approximately does.

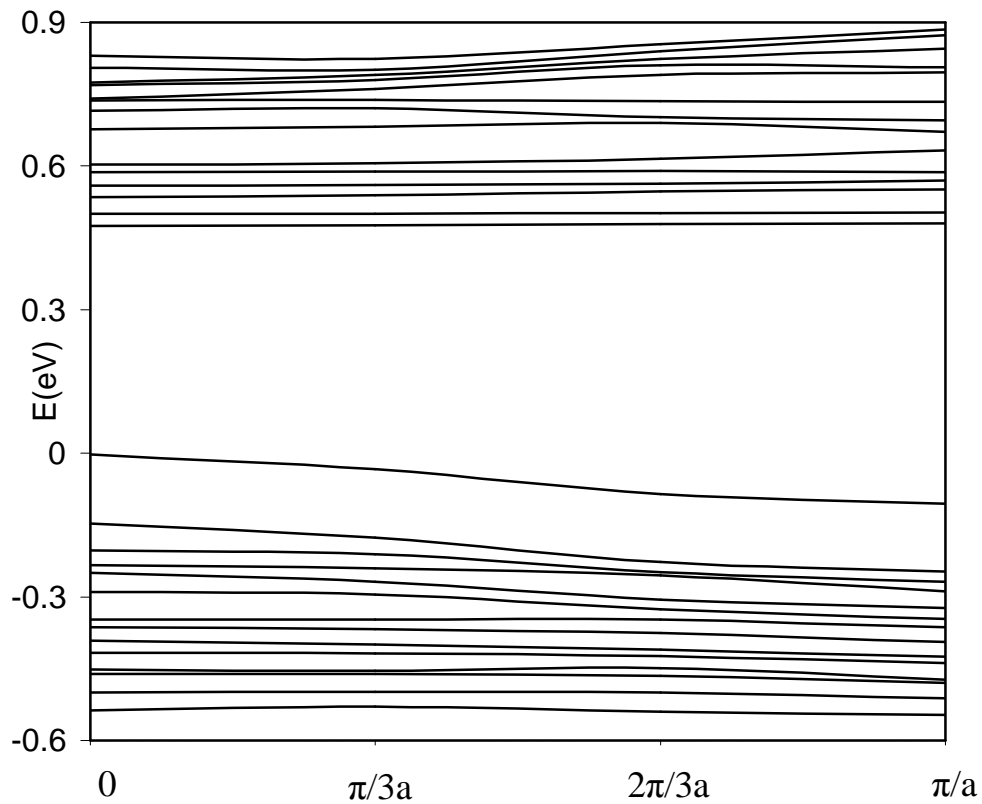


**Fig. 6.1.7: Si(001)/Si(100) energy bands in eV away from the top of the valence bands.**

The Si(001)/Si(100) energy bands are plotted in Fig. 6.1.7. There is very little dispersion, the highest valence band is the 560<sup>th</sup> and, in spite of the fact that band 560

looks as if it has been pushed out of the top of the valence bands, there are no interface states. This is consistent with there being no dangling bonds. The lack of dispersion is due, at least in part, to the longest BZ dimension being shorter than in configuration A by a factor of  $2^{-1/2}$ .

To summarize, we have calculated the interface and adhesion energies, the valence band offsets, the number of interface bands, and the interface widths of Si(110)/Si(001) and Si(001)/Si(100) junctions. Perhaps the most interesting of these is the number of interface bands, zero in Si(001)/Si(100) and 10 per interface two-dimensional unit cell in Si(110)/Si(001), containing four electrons each (this follows from the four missing valence bands). These electrons are expected, together with the band offsets (which are necessary to introduce the asymmetry) to play a major role in determining the theoretical I-V curves.

## References

1. Nicola A. Hill, *J. Phys. Chem.* **104**, 6694 (2000).
2. Nicola A. Hill and Alessio Filippetti, *J. Magn. Magn. Mater.* **242-245**, 976 (2002).
3. Ram Seshadri and Nicola Hill, *Chem. Mater.* **13**, 2892 (2001).
4. Claude Ederer and Nicola A. Spaldin, *Curr. Opin. Solid State Mater. Sci.* **9**, 128 (2006).
5. M. Gajek, M. Bibes, S. Fusil, K. Bouzehouane, J. Fontcuberta, A. Barthelemy, and A. Fert, *Cond-Mat/0606444*.
6. E. C. Subbarao, *Ferroelectrics* **5**, 267 (1973).
7. N. W. Ashcroft and N. D. Mermin, *Solid State Physics*, W. B. Saunders Company, Philadelphia, 1976.
8. C. Kittel, *Introduction to Solid State Physics*, John Wiley and Sons, New York, 2000.
9. R. M. Martin, "Comment on: Calculation of electric polarization in crystals", *Phys. Rev. B* **9**:1998 1974.
10. M. V. Berry, "Quantal phase factors accompanying adiabatic changes", *Proc. Roy. Soc. London A* **392**:45, 1984.
11. R. D. King-Smith and D. Vanderbilt, "Theory of polarization of crystalline solids", *Phys. Rev. B* **47**:1651-1654, 1993.
12. R. Resta, "Macroscopic polarization in crystalline dielectrics: the geometric phase approach", *Rev. Mod. Phys.* **66**: 899-915, 1994.

13. D. J. Thouless, M. Kohmoto, M. P. Nightingale, and M. den Nijs, “Quantized Hall conductance in a two-dimensional periodic potential”, Phys. Rev. Lett 49:405-408, 1982.
14. C. Herring, In magnetism IV, edited by G. Rado and H. Suhl, Academic Press, New York, 1966.
15. M. Schlüter, Phys. Rev. B **17**, 5044 (1978).
16. P. Hohenberg, and W. Kohn, Phys. Rev. **136**, B864 (1964).
17. M. Born and J. R. Oppenheimer, “Zur Quantentheorie der Molekeln”, Ann. Physik 84:457, 1927.
18. D. R. Hartree, “the waves mechanics of an atom with non-coulombic central field: parts I, II, III”, Proc. Cambridge Phil. Soc. 24:89, 111, 426, 1928.
19. W. Kohn, and L. J. Sham, Phys. Rev. **140**, A1133 (1965).
20. H. Hellmann. *Einführung in die Quantenchemie* (Deuticke, Leipzig, 1937).
21. R. P. Feynman, Physical Review, **56**, 340 (1939).
22. W. Kohn and L. J. Sham, Physical Review, **137**, A1697 (1965).
23. D. M. Ceperley and B. J. Alder, Physical Review Letters, **45**(7), 566 (1980).
24. J. P. Perdew, K. Burke, and M. Enzerhof, Phys. Rev. Lett. **77**, 3865 (1996).
25. M. Chen, K. A. Rubin, and R. W. Barton, Appl. Phys. Lett. **49**, 502 (1986).
26. T. Chattopadhyay, J. X. Boucherle, and H. G. von Schnering, J. Phys. C: Solid State Phys. **20**, 1431 (1987).
27. K.M. Rabe and J. D. Joannopoulos, Phys. Rev. B **36**, 6631 (1987).
28. J. M. Leger and A. M. Redon, J. Phys.: Condensed Matter **2**, 5655 (1990).

29. N. R. Serebryanaya, V. D. Blank, and V. A. Ivdenko, Phys. Lett. A **197**, 63 (1995).
30. S. S. Kabalkina, L. F. Vereshchagin, N. R. Serebryanaya, Sov. Phys. JETP **24**, 917 (1967).
31. A. Onodera, I. Sakamoto, and Y. Fujii, Phys. Rev. B **56**, 7935 (1997).
32. I. A. Kornev, L. Bellaïche, P. Bouvier, P.-E. Janolin B. Dkhil, and J. Kreisel, Phys. Rev. Lett. **95**, 196804 (2005).
33. C. M. I. Okoye, J. Phys.: Condensed Matter **14**, 8625 (2002).
34. P. E. Blöchl, Phys. Rev. B **50**, 17953 (1994).
35. G. Kresse and J. Furthmüller, Phys. Rev. B **54**, 11169 (1996) and Comput. Mater. Sci. **6**, 15 (1996).
36. P. E. Blöchl, O. Jepsen, and O. K. Andersen, Phys. Rev. B **49**, 16223 (1994).
37. The VASP code picks a stress criterion consistent with the selected force criterion but does not reveal it.
38. The primitive fcc lattice vector  $(a/2, a/2, 0)$  becomes  $[(1+\epsilon)a/2, (1+\epsilon)a/2, \epsilon a]$  under the trigonal distortion. The fcc  $(a, 0, 0)$  becomes  $(a, \epsilon a, \epsilon a)$ . The VASP code calculates the former, from which the components of the latter are easily obtained. Our LDA values for  $(1+\epsilon)a/2$  and  $\epsilon a$  are  $5.89897 \text{ \AA}$  and  $0.033243 \text{ \AA}$  respectively.
39. The VASP code subtracts spin unpolarized atomic energies from the crystal total energy to obtain an incorrect value of the cohesive energy. We have substituted LDA and GGA spin polarized atomic energies obtained from supercell calculations.
40. P. Vinet, J. Ferrante, J. H. Rose, and J. R. Smith, J. Geophys. Res. **92**, 9319 (1987).

41. B. R. Sahu and Leonard Kleinman, Phys. Rev. B **72**, 113106 (2005).
42. L. L. Chang, P. J. Stiles, and L. Esaki, IBM J. Res. Dev. **10**, 484 (1966).
43. J. C. Slater, Symmetry and Energy Bands in Crystals (Dorer, New York, 1965) page 418.
44. Tanaka and K. Shindo, JPS Japan **50**, 3349 (1981).
45. Actually,  $Z^*$  is the longitudinal (i.e. along the 3-fold axis) component of a two component tensor.
46. Since  $Z^*$  depends on the derivative of the polarization, a large  $Z^*$  can occur even if there is no polarization. A crude estimate of the derivative of the polarization may be obtained from  $P/\tau$  and results in  $Z^* = 15.22$  (LDA).
47. The various EOS have only four parameters, the equilibrium volume, energy, bulk modulus and its derivative. That four parameters, involving only the energy minimum can fit the entire  $E(V)$  curve as well as they do is impressive but because  $E_c^{\text{cube}}$  and  $E_c^{\text{trig}}$  are so nearly parallel around their crossing point, the EOS fits are incapable of finding the crossing point accurately. The nine point spline, because it has no EOS assumptions built into it, yields much more accurate fits.
48. N. Hur, S. Park, P. A. Sharma, J. S. Ahn, S. Guha, and S-W. Cheong, Nature **429**, 392 (2004)
49. T. Kimura, T. Goto, H. Shintani, K. Ishizaka, T. Arima, and Y. Tokura, Nature **426**, 55 (2003).
50. Ch. Binek and B. Doudin, J. Phys: Condens. Matter. **17**, L39 (2005).
51. Craig J. Fennie and Karin M. Rabe, Phys. Rev. Lett. **97**, 267602 (2006).



52. Spalding's picture is that the transition metal is ionized into a formally  $d^0$  state which obviously cannot be magnetic and then the O  $2p$ -electrons form covalent bonds with the empty  $d$ -states. Formal valences are extremely predictive, yet are often unrelated to the actual charge distribution in a crystal. We therefore prefer our picture which is that the TM  $d$ - and O  $2p$ -states are nearly degenerate (so no ionization) and a large Hamiltonian matrix element splits them into bonding and antibonding states. The reason they are not magnetic is essentially the same as the reason that the molecular bonds in  $H_2$  are not. A similar point of view is expressed by R. E. Cohen in Nature **358**, 136 (2000). Several polarization mechanisms are discussed by D. I. Khomskii in J. Mag. Mag. Mater.
53. F. Sugawara, S. Iida, Y. Syono, and S. Akimoto, J. Phys. Soc. Japan **25**, 1553 (1968).
54. B. B van Aken, T. T. M Palstra, A. Filippetti, and N. A. Spaldin, Nature Materials **3**, 164 (2004).
55. T. Shishidou, N. Mikamo, Y. Uratani, F. Ishii, and T. Oguchi, J. Phys.: Condens. Matter **16**, S5677 (2004).
56. Craig J. Fennie and Karin M. Rabe, Phys. Rev. B **72**, 100103 (2005).
57. A. A. Belik, S. Iikubo, T. Yokosawa, K. Kodama, N. Igawa, S. Shamoto, M. Azuma, M Takano, K. Kimoto, Y. Matsui, and E. Takayama-Muromachi, J. Am. Chem. Soc. **129**, 971. (2007).
58. See Ref. 15 for references to earlier work.
59. A. M. dos Santos, S. Parashar, A. R. Raju, Y. S. Zhao, A. K. Cheetham, and C. N. R. Rao, Solid State Commun. **122**, 49 (2002).

60. J. Wang, J. B. Neaton, H. Zheng, V. Nagarajan, S. B. Ogale, B. Liu, D. Viehland, V. Vaithyanathan, D. G. Scholm, U. V. Waghmare, N. A. Spalding, K. M. Rabe, M. Wuttig, and R. Ramesh, *Science* **229**, 1719 (2003)
61. K. Y. Yun, D. Ricinschi, T. Kanashima, M. Noda, and M. Okuyama.
62. J. B. Neaton, C. Ederer, U. V. Waghmare, N. A. Spalding, and K. M. Rabe, *Phys. Rev. B* **71**, 014113 (2005).
63. M. Azuma, K. Takata, T. Saito, S. Ishiwata, Y. Shimakawa, and M. Takano, *J. Am. Chem. Soc.* **127**, 8889 (2005).
64. M. Sakai, A. Masuno, D. Kan, M. Hashisaka, K. Takata, M. Azuma, M. Takano, and Y. Shimakawa, *Appl. Phys. Lett.* **90**, 072903 (2007).
65. Y. Uratani, T. Shishidou, F. Ishii, and T. Oguchi, *Physica B*, **383**, 9 (2006).
66. Priya Mahadevan, Alex Zunger, and D. D. Sarma, *Phys. Rev. Lett.* **93**, 177201 (2004).
67. O. Bengone, M. A. Louani, P. Blochl, and J. Hugel, *Phys. Rev. B* **62**, 16392 (2000).
68. This assumption is not really valid because  $U$  is a screened Coulomb integral and the screening depends on the environment.
69. The radii of the projection spheres around each kind of atom are Bi(1.635 Å), Mn(1.323 Å), Ni(1.085 Å) and O(0.900 Å).
70. F. Bertaut, F. forrat, and P. Fang, *C. R. Acad. Sci.* **256**, 1958 (1963).
71. V. A. Bokov, G. A. Smolenskiĭ, S. A. Kizhaev, and I. E. MyI'nikova, *Sov. Phys. Solid State* **5**, 2646 (1964).
72. I. G. Ismailzade and S. A. Kizhaev, *Sov. Phys. Solid State* **7**, 236 (1965).
73. J. Chappert, *Phys. Lett.* **18**, 229 (1965).

74. F. Sugawara, S. Iida, Y. Syono, and S. Akimoto, *J. Phys. Soc. Japan* **20**, 1529 (1965).
75. H. Chiba, T. Atou, Y. Syouno, *J. Solid State Chem.* **132**, 139 (1997).
76. T. Atou, H. Chiba, K. Ohoyama, Y. Yamaguichi, Y. Syouno, *J. Solid State Chem.* **145**, 639 (1999).
77. A. dos Santos, A. Cheetham, T. Atou, Y. Syouno, Y. Yamaguichi, K. Ohoyama, H. Chiba, C. Rao, *Phys. Rev. B* **66**, 064425 (2002).
78. E. Montanari, G. Calestani, A. Migliori, M. Dapiaggi, F. Bolzoni, R. Cabassi, and E. Gilioli, *Chem. Mater.* **17**, 6457 (2005).
79. E. Montanari, G. Calestani, L. Righi, E. Gilioli, F. Bolzoni, K. S. Knight, and P. G. Radaelli, *Phys. Rev. B* **75**, 220101 (2007).
80. P. Baettig, R. Seshadri and Nicola A. Spaldin, *J. Am. Chem. Soc.* **129**, 9854 (2007).
81. Adrian Ciucivara, Bhagawan Sahu and Leonard Kleinman, *Phys. Rev. B* **76**, 064412 (2007).
82. P. Murugravel, D. Saurel, W. Prellier, Ch. Simon, and B. Raveau, *Appl. Phys. Lett.* **85**, 4424 (2004).
83. M. P. Singh, W. Prellier, L. Mechin, Ch. Simon, B. Raveau, *Thin Solid Films* (2007), doi:10.1016/j.tsf.2006.11.059.
84. Chun-Gang Duan, S. S. Jaswal, E. Y. Tsybal, *Phys. Rev. Lett.* **97**, 047201 (2006).
85. Since nothing was said about the longitudinal lattice constant and the VASP code that they used requires all of the lattice constants to be fixed if one is, we assume they chose some approximate value for the longitudinal lattice constant.
86. K. Yamauchi, B. Sanyal, and S. Picozzi, *Appl. Phys. Lett.* **91**, 062506 (2007).

87. S. L. Dudarev, G. A. Botton, S. Y. Savrasov, C. J. Humphreys, and A. P. Sutton, Phys. Rev. B **57**, 1505 (1998).
88. A. E. Bocquet, T. Mizokawa, T. Saitoh, H. Namatame, and A. Fujimori, Phys. Rev. B **46**, 3771 (1992).
89. S. Satpathy, Zoran S. Popovic and Filip R. Vukajlovic, Phys. Rev. Lett. **76**, 960 (1996).
90. By layer we mean one LaO plane and one MnO<sub>2</sub> plane; the LaMnO<sub>3</sub> unit cell contains two such layers.
91. Landolt Bornstein New Series-Group III, vol. 16a, p. 67.
92. H. Sawada, Y. Morekawa, K. Terakura, and N. Hamada, Phys. Rev. B **56**, 12154 (1997) list the lattice constants but say not from where they came.
93. J. B. A. A. Elemans, B. van Laar, K. R. van der Veen, B. O. Loopstra, J. Solid State Chem. **3**, 238 (1971).
94. It is interesting to note that a very smooth curve can be drawn by subtracting 4, 3, 2, 1, and 0 quanta from the values with 100%, 75%, 50%, 25%, and 0% displacements, respectively, but there is no way to make the point at 10% displacement lie on that curve.
95. Na Sai, Alexie M. Kolpak, and Andrew M. Rappe, Phys. Rev. B **72**, 020101(R) (2005).
96. M. Yamada et al., J. Appl. Phys. **91**, 7908 (2002).
97. H. Saito, W. Zaets, S. Yamagata, Y. Suzuki, and K. Ando, J. Appl. Phys. **91**, 8085 (2002).
98. Gustavo M. Dalpian and Su-Huai Wei, Journal of Appl. Phys. **98**, 083905 (2005).

99. Priya Gopal and N. A. Spaldin, *Phys. Rev. B* **74**, 094418 (2006).
100. R. W. Cochrane, M. Plishke, J. O. Ström-Olsen *Phys. Rev. B* **9** 3013 (1974).
101. Y. Fukumura, T. Murakami, H. Asada, and T. Koyanagy, *Physica E* **10**, 273 (2001).
102. Y. Fukuma, H. Asada, J. Miyashita, N. Nishimura and T. Koyanagy, *J. Appl. Phys.* **93**, 7667 (2003).
103. Y. Fukuma, H. Asada, M. Arifuku and T. Koyanagy, *Appl. Phys. Lett.* **80**, 1013 (2002).
104. Y. Fukuma, M. Arifuku, H. Asada, and T. Koyanagi, *J. Appl. Phys.* **91**, 7502 (2002).
105. A. H. Edwards, A. C. Pineda, P.A. Schultz, M. G. Martin, A. P. Thompson, and H. P. Hjalmarson, *J. Phys.:Condens. Matter*.
106. The text of Ref. 8 says that the carrier concentration increases monotonically with Te composition, in contradiction to the tabulated data which Prof. Fukuma informs us is correct.
107. Adrian Ciucivara, B. R. Sahu and Leonard Kleinman, *Phys. Rev. B* **73**, 214105 (2006).
108. M. Yang, E. P. Gustov, M. Jeong, O. Gluschenkov, D. C. Boyd, K. K. Chan, P. M. Kozlowski, C. P. D. Emic, R. M. Sicina, M. Jeong, P. C. Jamison, and A. I. Chou, *IEEE Electron Device Letters* **24**, 453 (2003).
109. V. Fischetti, Z. Ren, P. M. Solomon, M. Yang, and K. Rim, *J. Appl. Phys.* **94**, 107 (2003).
110. K. L. Saenger, J. P. de Souza, K. E. Fogel, J. A. Ott, A. Reznicek, C. Y. Sung, D. K. Sadena and H. Yin, *Appl. Phys. Lett.* **87**, 221911 (2005).

111. S. Joshi, A. Ciucivara, B. Sahu, L. Kleinman, R. Wise, M. Seacrist, M. Ries, R. Cleavelin, A. Pinto, Y.-T. Huang, M. Ma, C.-T. Lin and S. K. Banerjee, *Appl. Phys. Lett.*
112. *Fig. 6.1* is a more recent measurement (than those reported in Ref. 111) on a junction that resulted in a somewhat greater asymmetry than did previously measured junctions, and we have expanded the low voltage region and obtained a much smoother curve by measuring many more data points.
113. The VASP code selects the strain convergence criterion thought to be comparable to the force criterion which has been selected.
114. C. Messmer and J. C. Bilello, *J. Appl. Phys.* **52**, 4623 (1981).

# VITA

Adrian Ioan Ciucivara was born in Semeac, Arad, Romania on December 30, 1976, the son of Ioan Ciucivara and Dorina Ciucivara. After completing his high school at Vasile Goldis, Arad, Romania, in 1995, he entered The West University of Timisoara where he received his B.S. in Physics in 1999 and later in 2001 he received his M.S. in Physics from The University of Bucharest. In August 2002 he entered the Graduate School of The University of Texas.

Permanent Address: 1906 Pearl Street, Austin, Texas, 78705 USA.

This dissertation was typed by the author.